KeAi
CHINESE ROOTS
GLOBAL IMPACT

Contents lists available at ScienceDirect

Petroleum Science

journal homepage: www.keaipublishing.com/en/journals/petroleum-science



Original Paper

Finite-difference simulation of elastic waves in fluid-solid coupled media with irregular interface



Xu-Hui Zhou^a, Yi-Yuan Wang^{a,b}, Shou-Dong Huo^{a,b,*}

- ^a Key Laboratory of Deep Petroleum Intelligent Exploration and Development, Institute of Geology and Geophysics, Chinese Academy of Sciences, Beijing, 100029 China
- ^b College of Earth and Planetary Sciences, University of the Chinese Academy of Sciences, Beijing, 100049, China

ARTICLE INFO

Article history: Received 7 March 2024 Received in revised form 28 March 2025 Accepted 23 June 2025 Available online 2 July 2025

Edited by Meng-Jiao Zhou

Keywords: Fluid-solid coupled media Boundary condition Irregular interface Numerical simulation Staircase diffraction noise

ABSTRACT

The finite-difference method (FDM) is an essential tool in exploration geophysics, particularly for simulating wave propagation in fluid-solid coupled media. Despite its widespread use, FDM faces significant challenges that affect its accuracy and efficiency. Firstly, the implicit handling of fluid-solid boundary conditions through parameter averaging strategy often results in low simulation accuracy. Secondly, surface topography can introduce staircase diffraction noise when grid spacing is large. To address these issues, this paper presents a novel approach. We derive an implicit expression for fluid-solid boundary conditions based on average medium theory, translating explicit boundary conditions into model parameter modification. This enables implicit handling of fluid-solid boundaries by modifying the parameters near the boundary. Furthermore, to mitigate staircase diffraction noise, we employ multiple interface discretization based on the superposition method. This effectively suppresses staircase diffraction noise without requiring grid refinement. The efficacy of our method in accurately modeling wave propagation phenomena in fluid-solid coupled media is demonstrated by numerical examples. Results align well with those obtained using the spectral element method (SEM), with significant reduction in staircase diffraction noise.

© 2025 The Authors. Publishing services by Elsevier B.V. on behalf of KeAi Communications Co. Ltd. This is an open access article under the CC BY-NC-ND license (http://creativecommons.org/licenses/by-nc-nd/4.0/).

1. Introduction

The study of seismic wave propagation in fluid-solid coupled media has garnered considerable attention across various scientific domains in recent years. This phenomenon poses a significant challenge in understanding the intricate interactions between fluid and solid mediums, where changes in fluid pressure induce deformations in solids, and conversely, solid deformations affect fluid behavior through the boundary interface linking the two media. The simulation of coupled fluid-solid media holds paramount importance in fields such as geophysics, engineering, and medicine. In exploration geophysics, it finds diverse applications ranging from marine reflected wave exploration to full-waveform inversion and hydraulic fracturing studies (Liang et al., 2017; Li

E-mail address: huoshoudong@mail.iggcas.ac.cn (S.-D. Huo).

Peer review under the responsibility of China University of Petroleum (Beijing).

et al., 2018; Agudo et al., 2020; Antonietti et al., 2020; Kamath et al., 2021; Yang et al., 2023; Xie et al., 2024a, 2024b). Engineering applications heavily rely on these simulations for dynamic assessments of structures such as dams (Soares and Mansur, 2006; Soares, 2008). Furthermore, medical research benefits from techniques like full waveform inversion in brain ultrasound studies (Guasch et al., 2020).

However, in many imaging and inversion studies, including full-waveform inversion and reverse-time migration, only the pressure recorded by hydrophones or the vertical component recorded by geophones is utilized. This selective use simplifies the treatment of the fluid-solid coupled medium into a single fluid medium and disregards the elastic properties of the solid medium, such as P-S converted waves and interface waves. Consequently, there is a significant loss of information regarding the complex interactions within the medium. To fully exploit the potential of recording devices such as Ocean Bottom Cable (OBC) or Ocean Bottom Node (OBN), it becomes imperative to accurately simulate and invert the propagation characteristics of the entire seismic wave field in the fluid-solid coupled system. This approach ensures

^{*} Corresponding author.

that the elastic characteristics of the subsurface solid medium, such as the S-wave velocity model, are properly captured in velocity inversion processes.

Numerical simulation methods for fluid-solid coupled media in geophysics are commonly categorized into two main types: partitioned and monolithic methods (Hou et al., 2012; De Basabe and Sen. 2015). The partitioned method employs different wave equations in the fluid and solid regions, explicitly addressing the fluid-solid boundary conditions. One advantage of this approach is its ability to reduce the number of degrees of freedom in the fluid domain, explicitly satisfying interface conditions, and even allowing for the use of different numerical methods in different domains (Komatitsch et al., 2000b; Carcione and Helle, 2004; Cao et al., 2022). However, it requires precise knowledge of the interface location, which can be cumbersome in cases of complex geometry. In contrast, the monolithic method utilizes the same wave equation for the entire fluid-solid coupling medium, implicitly incorporating interface conditions (Virieux, 1986; Graves, 1996; van Vossen et al., 2002). Its advantages lie in its simplicity of implementation and its applicability to any interface case. However, drawbacks include limitations in numerical simulation accuracy due to dispersion characteristics and the discretization of undulating interfaces. Despite the advantages of the partitioned method, the monolithic approach has been widely employed in exploration geophysics. Therefore, our study focuses on the monolithic method.

The staggered-grid FDM (Virieux, 1986) is widely utilized in the monolithic approach due to its ease of implementation, low memory requirements, and high computational efficiency. In modeling wave propagation within fluid-solid coupled media, this method typically sets only the shear velocity to zero in the fluid region and uses the harmonic averaging of shear module at the interface. However, its effectiveness is limited to a specific range of incidence angles (Graves, 1996). In addition, this simplified approach assumes that all field variables remain continuous at the fluid-solid interface, which differs from the fluid-solid boundary condition where the normal components of stress and displacement are continuous while the tangential components are discontinuous. Consequently, this assumption may lead to inaccurate energy partitioning, particularly concerning interface and converted waves (De Basabe and Sen, 2015). Furthermore, the discretization of surface topography poses a challenge in the application of FDM. Two commonly employed methods for addressing this issue are the grid deformation method and the rectangular grid method. The grid deformation method entails mapping a rectangular grid onto a curvilinear grid and implementing boundary conditions on the deformed grid. While this approach offers more accurate results, particularly for complex topographies, its implementation is inherently more complex and challenging (Tessmer and Kosloff, 1994; Zhang et al., 2012; de la Puente et al., 2014; Petersson and Sjogreen, 2015; Qu et al., 2017; Li et al., 2019; Sun et al., 2021).

To circumvent the necessity for grid deformation, many researchers opt for using rectangular grids to represent surface topography. Rectangular grids can be classified into two types: variable grids and regular grids. Variable grids employ varying grid spacing across different areas of the model, thereby avoiding oversampling and effectively reducing computational costs (Sun and Yang, 2003; Liu and Sen, 2011). In contrast, regular grids maintain uniform grid spacing throughout the model, which results in a spatial sampling strategy inside the model dependent on the strategy at the interface, consequently leading to increased computational costs, particularly when dealing with surface topography. Regular grids often employ a staircase approximation to represent surface topography (Robertsson, 1996; Kristek et al.,

2002; Zeng et al., 2012; Cao and Chen, 2018; Li et al., 2020; Zhou et al., 2023b; Chen et al., 2024). However, staircase approximation with large grid spacing can introduce non-correlated diffraction noise in the wavefront as it propagates into the staircase-shaped topography, affecting the wavefield record. While reducing the grid spacing effectively suppresses staircase diffraction noise, it entails larger computational costs and memory requirements. Addressing the issues of inaccurate expression of fluid-solid boundary conditions and staircase diffraction noise generated during surface topography discretization is imperative to enhance the applicability of FDM in fluid-solid coupled media.

Building upon the aforementioned challenges, this paper introduces an implicit expression of fluid-solid boundary conditions suitable for staggered-grid FDM from a physical point of view. The proposed expression is derived utilizing average medium theory, facilitating the realization of fluid-solid boundary conditions by modifying the constitutive relationship and density at the interface. Furthermore, the paper presents a discretization method for surface topography based on the superposition method (Drainville et al., 2019; Zhou et al., 2023b). This approach enables effective suppression of staircase diffraction noise even with larger grid spacing, thereby reducing computational costs and memory requirements significantly. Through a series of numerical experiments, the accuracy and effectiveness of the proposed method in suppressing staircase diffraction noise are demonstrated. These findings underscore the method's pivotal role in numerical simulations of fluid-solid coupled media.

2. Methods

2.1. Derivation of the fluid-solid boundary condition

Based on the average medium theory proposed by Moczo et al. (2002), this paper derives a novel expression for fluid-solid boundary conditions from a physical perspective, utilizing the constitutive relationship between two isotropic solid media. This expression can be directly applied to the velocity-stress staggeredgrid FDM, which is currently mainstream in the industry. In accordance with the average medium theory, as illustrated in Fig. 1, the effective representation of two interconnected isotropic elastic media can be achieved through an averaged medium. The averaged medium can be mathematically expressed as

$$\boldsymbol{\tau}^{\mathbf{A}} = \mathbf{E}^{\mathbf{A}} \boldsymbol{\varepsilon}^{\mathbf{A}},\tag{1}$$

where τ^A and ε^A are the stress and strain tensor of the averaged medium, respectively, which can also be understood as the stress and strain tensor at the interface where the two media are connected, and \mathbf{E}^A is the elasticity matrix of the averaged medium,

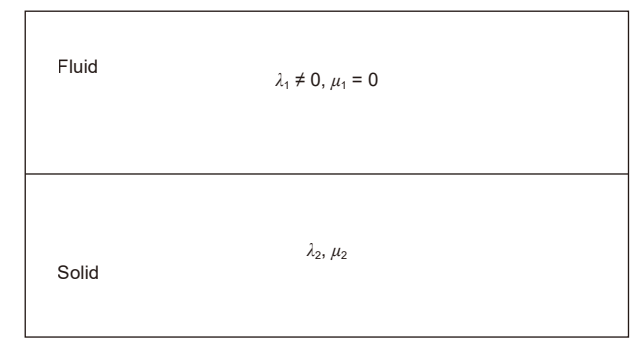


Fig. 1. Schematic diagram of the elastic parameters at the fluid-solid interface.

which contains only the elasticity parameters (λ_1, μ_1) and (λ_2, μ_2) of the upper and lower media, where λ and μ are the Lamé constants. Since the stress and displacement continuity conditions cannot be satisfied at the fluid-solid interface, it is not possible to directly generalize the average medium method proposed by Moczo et al. (2002) that is suitable for the solid-solid interface to the fluid-solid interface. Therefore, we start the derivation from the physical point of view, first posit a solid-solid interface, and derive the constitutive relation of this solid-solid interface according to the theory of the average medium method. On the basis of this constitutive relationship, the shear modulus of a certain layer of medium is equal to zero (i.e., $\mu_1 = 0$), so that the physical properties of the interface approximate to the fluid-solid interface, which can establish the constitutive relationship at the fluid-solid interface. This kind of method has been successfully applied to the free surface scenario (Mittet, 2002; Xu et al., 2007; Cao et al., 2018; Zhou et al., 2022, 2023a), and thus the method can be used to carry out the treatment of fluid-solid interfaces as well from the physical point of view. The proposed method can implicitly implement boundary conditions by modifying model parameters at the fluidsolid interface.

We elaborate on our derivation process using the example of isotropic media in two-dimensional scenarios. The constitutive relations of isotropic media can be expressed as

$$\begin{bmatrix} \tau_{XX} \\ \tau_{ZZ} \\ \tau_{XZ} \end{bmatrix} = \begin{bmatrix} \lambda + 2\mu & \lambda & 0 \\ \lambda & \lambda + 2\mu & 0 \\ 0 & 0 & \mu \end{bmatrix} \begin{bmatrix} \varepsilon_{XX} \\ \varepsilon_{ZZ} \\ 2\varepsilon_{XZ} \end{bmatrix}. \tag{2}$$

According to the displacement and stress continuity conditions at the interface (Alterman and Karal Jr, 1968; Moczo et al., 2002), the stress and strain components can be classified into two categories: continuous and discontinuous components, which are represented by Eqs. (3) and (4), respectively:

$$\tau_{C} = [\tau_{XZ}, \tau_{ZZ}],
\varepsilon_{C} = [\varepsilon_{XX}],$$
(3)

and

where the subscript c represents the continuous component, while the subscript d represents the discontinuous component. Combining Eqs. (2)–(4), the elasticity matrix is readjusted to obtain an alternative expression of the constitutive relationship at the interface:

$$\begin{bmatrix} \boldsymbol{\tau}_{\mathsf{C}} \\ \boldsymbol{\tau}_{\mathsf{d}} \end{bmatrix} = \begin{bmatrix} \mathbf{R} & \mathbf{P} \\ \mathbf{P}^{\mathsf{T}} & \mathbf{S} \end{bmatrix} \begin{bmatrix} \boldsymbol{\varepsilon}_{\mathsf{d}} \\ \boldsymbol{\varepsilon}_{\mathsf{c}} \end{bmatrix}, \tag{5}$$

with

$$\mathbf{R} = \begin{bmatrix} \mu & 0 \\ 0 & \lambda + 2\mu \end{bmatrix}, \quad \mathbf{P} = \begin{bmatrix} 0 \\ \lambda \end{bmatrix}, \tag{6}$$

$$\mathbf{S} = [\lambda + 2\mu].$$

By placing the discontinuous component of the above equation on the left-hand side of the equal sign, we can rewrite Eq. (5) as

$$\begin{bmatrix} \boldsymbol{\varepsilon}_{\mathrm{d}} \\ \boldsymbol{\tau}_{\mathrm{d}} \end{bmatrix} = \begin{bmatrix} -\mathbf{R}^{-1}\mathbf{P} & \mathbf{R}^{-1} \\ \mathbf{S} - \mathbf{P}^{\mathrm{T}}\mathbf{R}^{-1}\mathbf{P} & \mathbf{P}^{\mathrm{T}}\mathbf{R}^{-1} \end{bmatrix} \begin{bmatrix} \boldsymbol{\varepsilon}_{\mathrm{c}} \\ \boldsymbol{\tau}_{\mathrm{c}} \end{bmatrix}. \tag{7}$$

Based on Eq. (7), we next introduce the average medium theory. Assuming that D is the discontinuous function at the interface, i.e., $\mathbf{D}^1 \neq \mathbf{D}^2$, we define the averaging function \mathbf{D}^A to be

$$\mathbf{D}^{\mathbf{A}} \stackrel{1}{=} \frac{1}{2} \left(\mathbf{D}^1 + \mathbf{D}^2 \right). \tag{8}$$

According to Eqs. (1) and (8), the discontinuity component of the averaged medium can be expressed as

$$\begin{bmatrix} \boldsymbol{\varepsilon}_{d}^{A} \\ \boldsymbol{\tau}_{d}^{A} \end{bmatrix} = \begin{bmatrix} \left(-\mathbf{R}^{-1} \mathbf{P} \right)^{A} & \left(\mathbf{R}^{-1} \right)^{A} \\ \left(\mathbf{S} - \mathbf{P}^{T} \mathbf{R}^{-1} \mathbf{P} \right)^{A} & \left(\mathbf{P}^{T} \mathbf{R}^{-1} \right)^{A} \end{bmatrix} \begin{bmatrix} \boldsymbol{\varepsilon}_{c}^{A} \\ \boldsymbol{\tau}_{c}^{A} \end{bmatrix}, \tag{9}$$

with

$$\begin{bmatrix} \boldsymbol{\varepsilon}_{\mathrm{d}}^{\mathrm{A}} \\ \boldsymbol{\tau}_{\mathrm{d}}^{\mathrm{A}} \end{bmatrix} = \frac{1}{2} \begin{pmatrix} \begin{bmatrix} \boldsymbol{\varepsilon}_{\mathrm{d}}^{1} \\ \boldsymbol{\tau}_{\mathrm{d}}^{1} \end{bmatrix} + \begin{bmatrix} \boldsymbol{\varepsilon}_{\mathrm{d}}^{2} \\ \boldsymbol{\tau}_{\mathrm{d}}^{2} \end{bmatrix} \end{pmatrix}, \quad \begin{bmatrix} \boldsymbol{\varepsilon}_{\mathrm{c}}^{\mathrm{A}} \\ \boldsymbol{\tau}_{\mathrm{c}}^{\mathrm{A}} \end{bmatrix} = \begin{bmatrix} \boldsymbol{\varepsilon}_{\mathrm{c}}^{1} \\ \boldsymbol{\tau}_{\mathrm{c}}^{1} \end{bmatrix} = \begin{bmatrix} \boldsymbol{\varepsilon}_{\mathrm{c}}^{2} \\ \boldsymbol{\tau}_{\mathrm{c}}^{2} \end{bmatrix}. \quad (10)$$

We bring $\varepsilon_{\rm d}^{\rm A}, \varepsilon_{\rm c}^{\rm A}, \tau_{\rm d}^{\rm A}$, and $\tau_{\rm d}^{\rm A}$ into Eq. (7) and replace $\varepsilon_{\rm d}, \varepsilon_{\rm c}, \tau_{\rm d}$, and $\tau_{\rm c}$ accordingly. Afterwards, by placing the stress components on the left-hand side of the equal sign, we obtain

$$\begin{bmatrix} \boldsymbol{\tau}_{c}^{A} \\ \boldsymbol{\tau}_{d}^{A} \end{bmatrix} = \begin{bmatrix} \overline{\mathbf{R}} \\ \overline{\mathbf{P}}^{I} & \overline{\mathbf{S}} \end{bmatrix} \begin{bmatrix} \boldsymbol{\varepsilon}_{d}^{A} \\ \boldsymbol{\varepsilon}_{c}^{A} \end{bmatrix}, \tag{11}$$

with

$$\overline{\mathbf{R}} = \left[\left(\mathbf{R}^{-1} \right)^{\mathbf{A}} \right]^{-1},
\overline{\mathbf{P}} = \left[\left(\mathbf{R}^{-1} \right)^{\mathbf{A}} \right]^{-1} \left(\mathbf{R}^{-1} \mathbf{P} \right)^{\mathbf{A}},
\overline{\mathbf{S}} = \left(\mathbf{S} - \mathbf{P}^{\mathsf{T}} \mathbf{R}^{-1} \mathbf{P} \right)^{\mathbf{A}} + \left(\mathbf{P}^{\mathsf{T}} \mathbf{R}^{-1} \right)^{\mathbf{A}} \left[\left(\mathbf{R}^{-1} \right)^{\mathbf{A}} \right]^{-1} \left(\mathbf{R}^{-1} \mathbf{P} \right)^{\mathbf{A}}.$$
(12)

Recombining the above equation according to Eq. (2) yields

$$\begin{bmatrix} \tau_{XX} \\ \tau_{ZZ} \\ \tau_{XZ} \end{bmatrix} = \begin{bmatrix} \frac{2\mu_{1}(\lambda_{1} + \mu_{1})}{\lambda_{1} + 2\mu_{1}} + \frac{2\mu_{2}(\lambda_{2} + \mu_{2})}{\lambda_{2} + 2\mu_{2}} + \eta & \frac{\lambda_{1}(\lambda_{2} + 2\mu_{2}) + \lambda_{2}(\lambda_{1} + 2\mu_{1})}{\lambda_{1} + 2\mu_{1} + \lambda_{2} + 2\mu_{2}} & 0 \\ \frac{\lambda_{1}(\lambda_{2} + 2\mu_{2}) + \lambda_{2}(\lambda_{1} + 2\mu_{1})}{\lambda_{1} + 2\mu_{1} + \lambda_{2} + 2\mu_{2}} & \frac{2(\lambda_{1} + 2\mu_{1})(\lambda_{2} + 2\mu_{2})}{\lambda_{1} + 2\mu_{1} + \lambda_{2} + 2\mu_{2}} & 0 \\ 0 & 0 & \frac{4\mu_{1}\mu_{2}}{\mu_{1} + \mu_{2}} \end{bmatrix} \begin{bmatrix} \varepsilon_{XX} \\ \varepsilon_{ZZ} \\ \varepsilon_{XZ} \end{bmatrix},$$

$$(13)$$

where

$$\eta = \frac{\left[\lambda_1(\lambda_2 + 2\mu_2) + \lambda_2(\lambda_1 + 2\mu_1)\right]^2}{2(\lambda_1 + 2\mu_1)(\lambda_2 + 2\mu_2)(\lambda_1 + 2\mu_1 + \lambda_2 + 2\mu_2)}.$$
 (14)

As shown in Fig. 1, in Eq. (13), by making the shear modulus $\mu_1 = 0$ in one of the layers of the medium, we can obtain the constitutive relationship satisfied by the stress and strain components at the fluid-solid interface from the physical point of view:

interface following the staircase approximation, we implement the grid configuration proposed by Kristek et al. (2002). Specifically, normal stresses are positioned at the interface, while shear stresses are placed half a grid point below the interface, as illustrated in Fig. 2. Regarding the required model parameters at the half-grid points, we adopt the strategy that harmonically averaging the Lamé constant and arithmetically averaging the density.

From Fig. 2, we observe that grid cells on the fluid-solid interface following the staircase approximation fall into seven major

$$\begin{bmatrix} \tau_{XX} \\ \tau_{ZZ} \\ \tau_{XZ} \end{bmatrix} = \begin{bmatrix} \frac{2\mu_{2}(\lambda_{2} + \mu_{2})}{\lambda_{2} + 2\mu_{2}} + \frac{[\lambda_{1}(\lambda_{2} + 2\mu_{2}) + \lambda_{2}\lambda_{1}]^{2}}{2\lambda_{1}(\lambda_{2} + 2\mu_{2})(\lambda_{1} + \lambda_{2} + 2\mu_{2})} & \frac{\lambda_{1}(\lambda_{2} + 2\mu_{2}) + \lambda_{2}\lambda_{1}}{\lambda_{1} + \lambda_{2} + 2\mu_{2}} & 0 \\ \frac{\lambda_{1}(\lambda_{2} + 2\mu_{2}) + \lambda_{2}\lambda_{1}}{\lambda_{1} + \lambda_{2} + 2\mu_{2}} & \frac{2\lambda_{1}(\lambda_{2} + 2\mu_{2})}{\lambda_{1} + \lambda_{2} + 2\mu_{2}} & 0 \\ 0 & 0 & 0 \end{bmatrix} \begin{bmatrix} \varepsilon_{XX} \\ \varepsilon_{ZZ} \\ \varepsilon_{XZ} \end{bmatrix}.$$

$$(15)$$

From this, we can see that the fluid-solid boundary condition is implicitly expressed in the elastic matrix of the fluid-solid averaged medium. As for the density at the fluid-solid interface, we refer to the treatment of Moczo et al. (2002) and use the arithmetic averaging method, that is

$$\rho = \frac{\rho_1 + \rho_2}{2} \,. \tag{16}$$

Eqs. (15) and (16) together give an implicit expression of the fluid-solid boundary conditions based on the average medium theory.

2.2. Extend the proposed method to topography scenarios

To effectively apply the proposed implicit expressions to fluid-solid interfaces with topography, we must extend the implicit expressions of boundary conditions derived from horizontal fluid-solid boundaries. This extension is necessary for ensuring applicability to arbitrarily complex fluid-solid interface geometries, as depicted in Fig. 2. For discretizing the irregular interface, we employ a staircase approximation. To maintain the overall position of the fluid-solid

classes: H, VL, VR, OL, OR, IL, and IR. Among these, H, VL, and VR denote grid cells for the fluid on the upper, left, and right sides of the interface respectively. OL and OR, as well as IL and IR, represent transition corner point cells of the interface. In the preceding section, we derived the implicit expression of the fluid-solid boundary condition at the horizontal interface, corresponding to the H grid cell. A schematic of the grid configuration and coordinate system utilized in the Finite Difference Method (FDM) is depicted in Fig. 3, where i and k denote the corresponding grid nodes in the x- and z-directions, i.e., $i = ih_x$, $k = ih_z$, with h_x and h_z denoting the grid spacing in the x- and z-directions respectively. As depicted in Fig. 3(b) and (c), we can transform a VL or VR grid cell into an H grid cell by rotating the VL or VR interface cell by an appropriate angle. For instance, considering the VL grid cell, rotating the coordinate system clockwise by 90° would convert the VL grid cell into an H grid cell in the new coordinate system. Consequently, we can extend the stress and strain relationship established on the H grid cell to the VL and VR grid cell by rotating the coordinate system. During coordinate rotation, the stress and strain components before and after rotation can be expressed as follows:

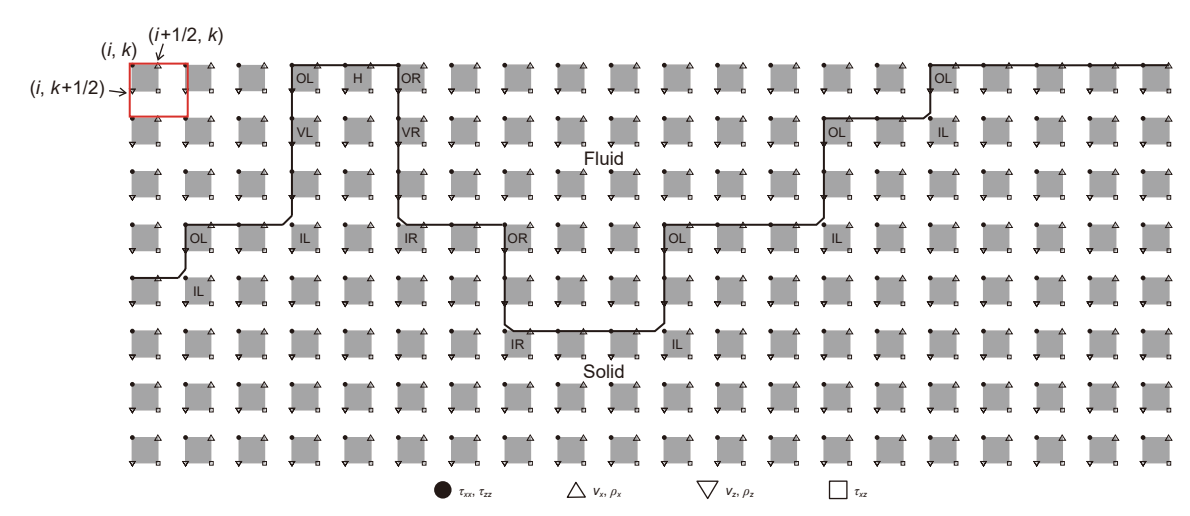


Fig. 2. The implementation of the topography of the proposed method. The squares represent the grid cells, and the solid circle indicates the positions of the integer grid point. The black line represents the irregular free surface obtained by staircase discretization. IL and IR indicate the inner corner grid cells with air above to the left and right, respectively; OL and OR indicate the outer corner grid cells with air to the left and right, respectively; VL and VR indicate the vertical boundary grid cells with air to the left and right, respectively; and H indicates the horizontal boundary grid cells.

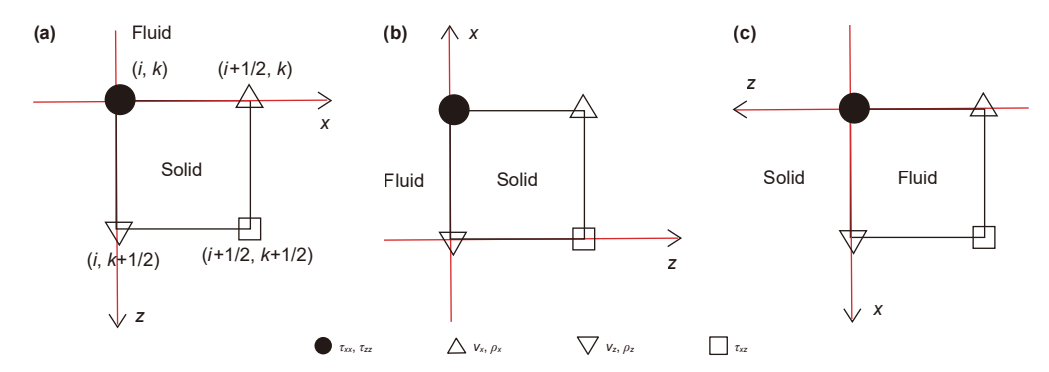


Fig. 3. Three kinds of boundary grid after the staircase discretization of the irregular fluid-solid interface. The red line in each subplot denotes the irregular fluid-solid interface. (a) H boundary grids: horizontal boundary grid used in the horizontal interface. (b) and (c) represent VL and VR boundary grids, which means vertical boundary grids with fluid to the left and right, respectively.

$$\begin{pmatrix} \tau'_{XX} & \tau'_{XZ} \\ \tau'_{ZX} & \tau'_{ZZ} \end{pmatrix} = \begin{pmatrix} \cos(\theta) & \sin(\theta) \\ -\sin(\theta) & \cos(\theta) \end{pmatrix} \begin{pmatrix} \tau_{XX} & \tau_{XZ} \\ \tau_{ZX} & \tau_{ZZ} \end{pmatrix}
\begin{pmatrix} \cos(\theta) & -\sin(\theta) \\ \sin(\theta) & \cos(\theta) \end{pmatrix},$$
(17)

and

$$\begin{pmatrix}
\varepsilon'_{XX} & \varepsilon'_{XZ} \\
\varepsilon'_{ZX} & \varepsilon'_{ZZ}
\end{pmatrix} = \begin{pmatrix}
\cos(\theta) & \sin(\theta) \\
-\sin(\theta) & \cos(\theta)
\end{pmatrix} \begin{pmatrix}
\varepsilon_{XX} & \varepsilon_{XZ} \\
\varepsilon_{ZX} & \varepsilon_{ZZ}
\end{pmatrix}$$

$$\begin{pmatrix}
\cos(\theta) & -\sin(\theta) \\
\sin(\theta) & \cos(\theta)
\end{pmatrix},$$
(18)

respectively.

In the above equations, θ represents the angle of rotation of the coordinate system, where positive values denote clockwise rotation. For the H grid cell, the constitutive relation can be observed in Eq. (15). Considering the VL grid cell as an example, from Eqs. (17) and (18), we obtain:

is needed; only an arithmetic averaging of the density is sufficient. In this way we obtain an expression of the boundary conditions at the irregular fluid-solid interface, which is also implicitly expressed in the elasticity matrix of the fluid-solid averaged medium. In the staggered-grid FDM, we transform the implicit expression of this irregular fluid-solid boundary into a modification of the model parameters at the grid points near the fluid-solid interface rerfering to Eqs. (19) and (20).

The derivation process outlined above illustrates that the proposed method of implicitly realizing fluid-solid boundary conditions can be readily extended to anisotropic and viscoelastic media by appropriately modifying Eq. (5) to accommodate different media types. Moreover, the proposed method can be straightforwardly extended to the three-dimensional case, meeting the requirements of large-scale numerical simulations.

2.3. Introduction of the superposition method

Generally, in order to suppress the staircase diffraction noise

$$\begin{bmatrix} \tau_{zz} \\ \tau_{xx} \\ \tau_{zx} \end{bmatrix} = \begin{bmatrix} \frac{2\mu_{2}(\lambda_{2} + \mu_{2})}{\lambda_{2} + 2\mu_{2}} + \frac{[\lambda_{1}(\lambda_{2} + 2\mu_{2}) + \lambda_{2}\lambda_{1}]^{2}}{2\lambda_{1}(\lambda_{2} + 2\mu_{2})(\lambda_{1} + \lambda_{2} + 2\mu_{2})} & \frac{\lambda_{1}(\lambda_{2} + 2\mu_{2}) + \lambda_{2}\lambda_{1}}{\lambda_{1} + \lambda_{2} + 2\mu_{2}} & 0 \\ \frac{\lambda_{1}(\lambda_{2} + 2\mu_{2}) + \lambda_{2}\lambda_{1}}{\lambda_{1} + \lambda_{2} + 2\mu_{2}} & \frac{2\lambda_{1}(\lambda_{2} + 2\mu_{2})}{\lambda_{1} + \lambda_{2} + 2\mu_{2}} & 0 \\ 0 & 0 & 0 \end{bmatrix} \begin{bmatrix} \varepsilon_{zz} \\ \varepsilon_{xx} \\ -\varepsilon_{xz} \end{bmatrix}.$$
(19)

Similarly, for the VR grid, we can obtain the corresponding constitutive relations by rotating the coordinates, that is

caused by the staircase discretization of irregular interfaces, the commonly used method is grid refinement, i.e., a smaller grid is

$$\begin{bmatrix} \tau_{zz} \\ \tau_{xx} \\ -\tau_{zx} \end{bmatrix} = \begin{bmatrix} \frac{2\mu_{2}(\lambda_{2} + \mu_{2})}{\lambda_{2} + 2\mu_{2}} + \frac{[\lambda_{1}(\lambda_{2} + 2\mu_{2}) + \lambda_{2}\lambda_{1}]^{2}}{2\lambda_{1}(\lambda_{2} + 2\mu_{2})(\lambda_{1} + \lambda_{2} + 2\mu_{2})} & \frac{\lambda_{1}(\lambda_{2} + 2\mu_{2}) + \lambda_{2}\lambda_{1}}{\lambda_{1} + \lambda_{2} + 2\mu_{2}} & 0 \\ \frac{\lambda_{1}(\lambda_{2} + 2\mu_{2}) + \lambda_{2}\lambda_{1}}{\lambda_{1} + \lambda_{2} + 2\mu_{2}} & \frac{2\lambda_{1}(\lambda_{2} + 2\mu_{2})}{\lambda_{1} + \lambda_{2} + 2\mu_{2}} & 0 \\ 0 & 0 & 0 \end{bmatrix} \begin{bmatrix} \varepsilon_{zz} \\ \varepsilon_{xx} \\ \varepsilon_{xz} \end{bmatrix}.$$
(20)

As for the density, its abrupt changes in the fluid and solid regions are small compared to the velocity, and no special treatment

used to discretize the irregular interfaces. However, grid refinement leads to a significant increase in computation costs, which

can lead to a significant reduction in computational efficiency and even the problem that the computer server is unable to satisfy the memory requirements of the computation.

Hence, this paper adopts the superposition method, as proposed by Drainville et al. (2019), to tackle the challenging issue of suppressing staircase noise. This involves applying the superposition theory to the discretization of irregular fluid-solid interfaces. According to the superposition theory, for a linear system, the overall state can be decomposed into a sum of independent parts. In this context, the equations can be solved independently in each of these parts, and subsequently, these independent solutions can be combined to obtain the overall solution. Traditionally, discretization of the staircase approximation employs a rounded grid division approach. Specifically, when the interface intersects a grid, if the area below the interface constitutes more than 50 percent of the grid, it is identified as the medium below the interface; conversely, if the area above the interface exceeds 50

percent, it is recognized as the medium above the interface. This straightforward division method is susceptible to generating staircase diffraction noise, especially when the grid spacing is considerable. To address this issue, we introduce several different thresholds for dividing the grids belonging to the interface. Assuming the total number of superpositions is denoted as N, the thresholds are set as $\frac{1}{N+1}, \frac{2}{N+1}, \dots, \frac{N}{N+1}$. Consequently, when the area of the grid below the interface exceeds a particular threshold, the grid is designated as part of the medium in the lower section. This concept can be succinctly expressed as follows:

$$\kappa_{\mathbf{n}}(x,z) = \begin{cases} 1 & \alpha(x,z) > \frac{n}{N+1} \\ 0 & \alpha(x,z) \le \frac{n}{N+1} \end{cases}$$
(21)

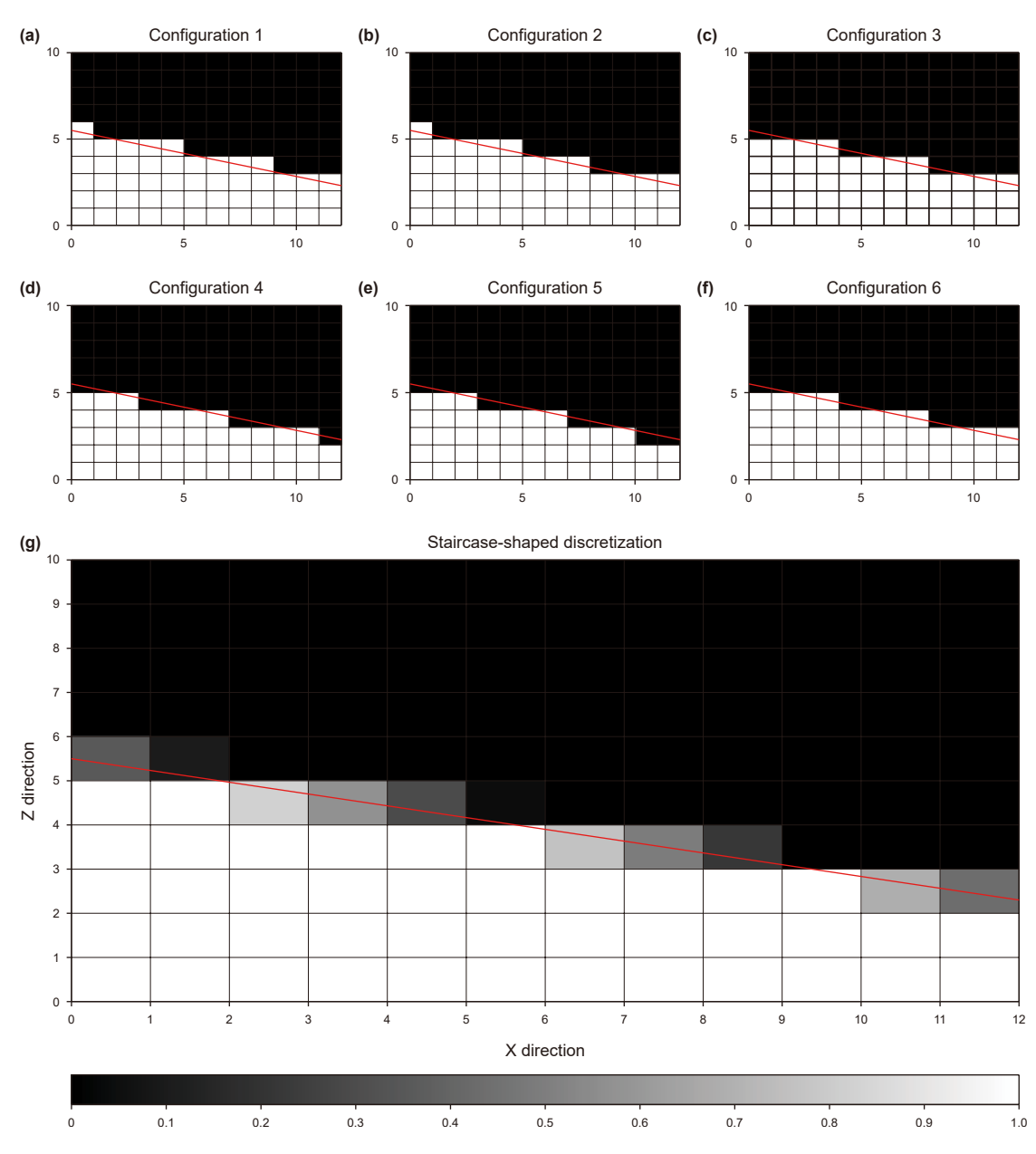


Fig. 4. Diagram of the superposition method when the number of superpositions is 6. Subplots (a)—(f) denote the discretization of irregular interface based on thresholds of 1/7, 2/7, 3/7, 4/7, 5/7, and 6/7, respectively. Subplot (g) indicates a schematic representation of irregular interface as it passes through the grid, with the color within each grid representing the size of the area of the grid region below the interface.

where $\kappa_n(x,z)$ represents the physical properties of the medium in the grid. While $\kappa_n(x,z)$ is 1, it represents that the grid belongs to the medium in the part below the interface, and when it is 0 it represents that the grid belongs to the medium in the part above the interface. $\alpha(x,z)$ represents the area of the grid in the part below the interface as a percentage of the total grid area. n is the nth

superposition. Taking N = 6 as an example, we give the discretization of the irregular fluid-solid interface for different thresholds in Fig. 4.

Based on this approach, we discretize the irregular interface N times and subsequently conduct numerical simulations for each discretization outcome. Finally, we superimpose the results

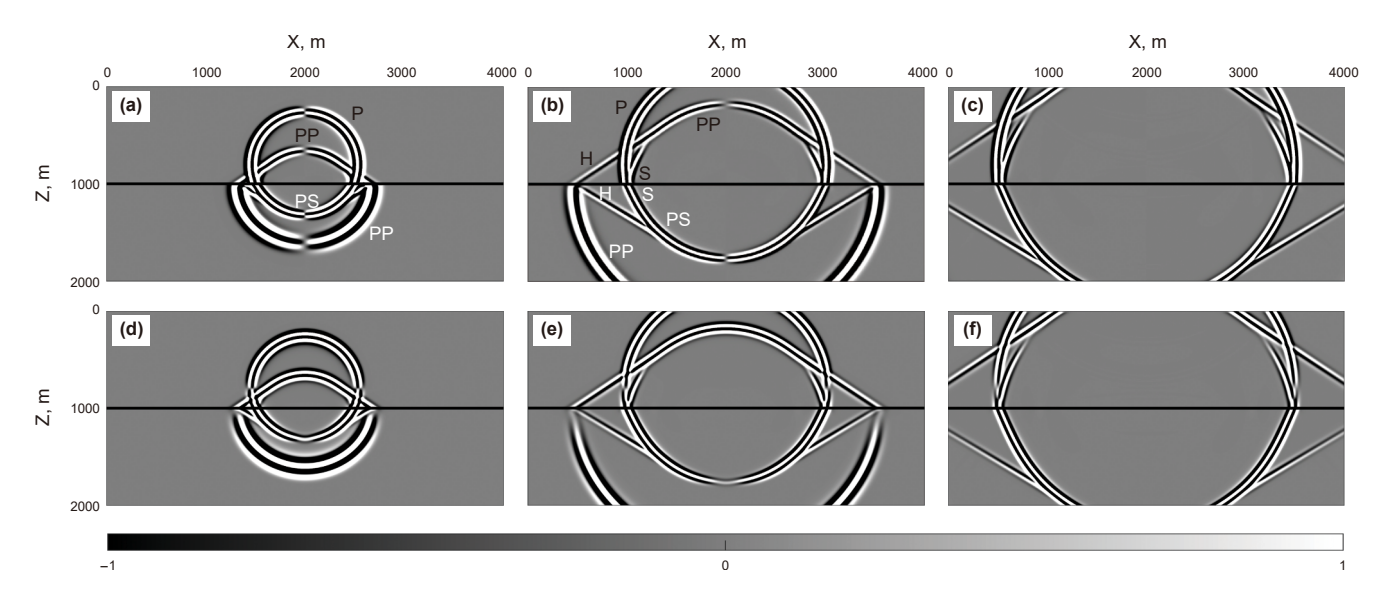


Fig. 5. Snapshots of the wavefield for the horizontal and vertical components of the particle velocity at different moments. The first row corresponds to the horizontal component of the particle velocity and the second row to the vertical component of the particle velocity. Subplots (a), (b) and (c) correspond to wavefield snapshots at t = 0.48 s, t = 0.80 s and t = 1.12 s, respectively. The black characters in the figure represent the wave phenomena present in the fluid part, while the white represents the solid part. P represents direct acoustic waves, PP represents reflected P and transmitted P waves, PS represents converted S waves, H represents the head wave associated with the transmitted P wave, and S represents Scholte waves.

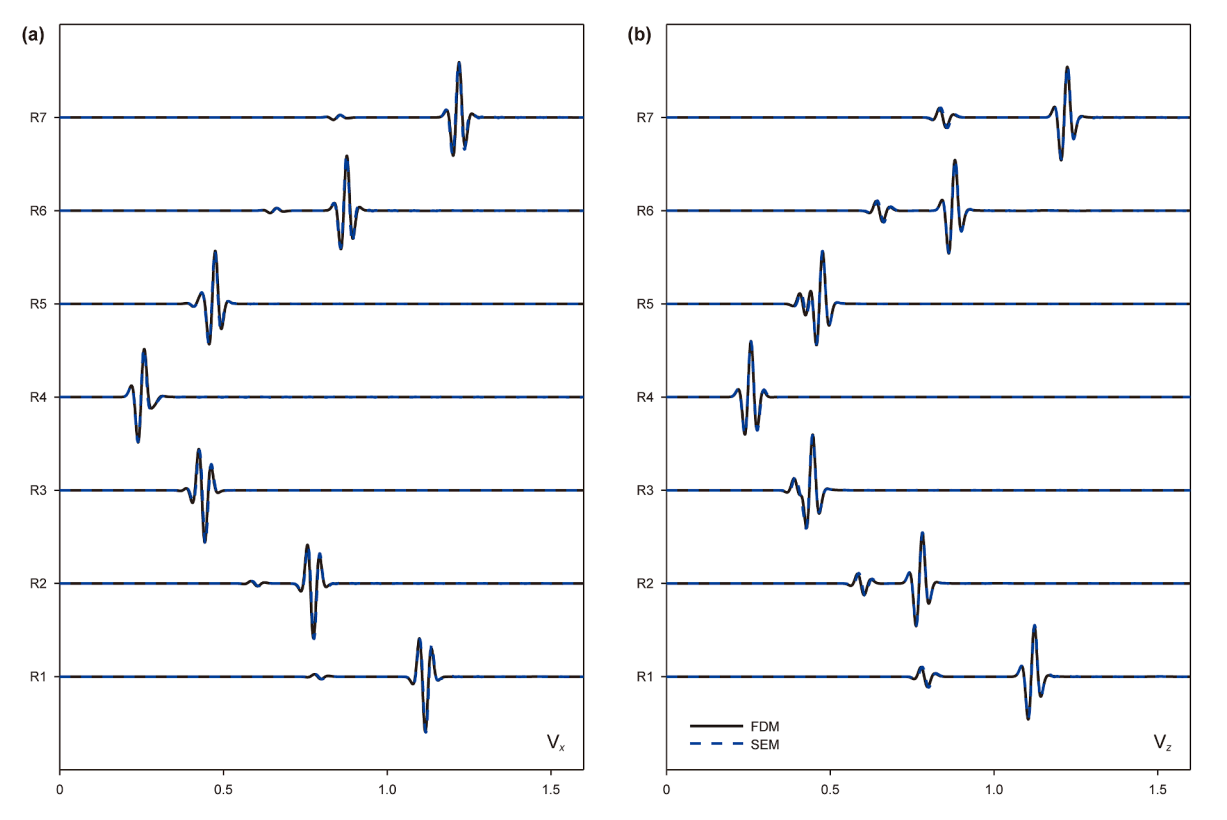


Fig. 6. Comparison of single-trace seismic records at different offset distances. Subplot (a) shows the comparison of the horizontal component of the particle velocity and subplot (b) shows the vertical component of the particle velocity.

corresponding to each discretization model to obtain the final simulation result, which can be expressed as

$$v(x,z,t) = \frac{1}{N} \sum_{n=1}^{N} v(x,z,t,n).$$
 (22)

3. Numerical experiments

In this section, we will present several numerical experiments to showcase the accuracy and viability of the proposed method. In our staggered-grid FD scheme, sixth-order spatial operators and second-order temporal operators were employed.

3.1. Case 1: a horizontal fluid-solid interface model

First, we validate our implicit expression of the fluid-solid boundary conditions through numerical experiments with two different horizontal interface fluid-solid bilayer models.

In Model 1, the dimensions are 4000 m \times 2000 m, with a discretized grid of 1001 \times 501 and a grid spacing of 4 m. In the solid part, the P-wave velocity is 2700 m/s, the S-wave velocity is 1400 m/s, and the density is 1200 kg/m³. In the fluid part, the P-wave velocity is 1500 m/s, and the density is 1000 kg/m³. The pressure source is located in the fluid at a depth of 800 m, positioned 200 m above the fluid-solid interface. We utilize a Ricker

wavelet as the source wavelet, with a dominant frequency of 17 Hz. The wavelet is recorded for a duration of 1.6 s, with a time step of 0.4 ms. Horizontal arrays of receivers are placed 20 m above the fluid-solid interface, with a spacing of 4 m between them. The horizontal and vertical components of wavefield snapshots at different time steps obtained from simulations are depicted in Fig. 5. These wavefield snapshots demonstrate that the proposed method effectively captures wave phenomena at the interface. To further validate the proposed implicit expression of fluid-solid boundary conditions and ensure accurate partitioning of energy between interface waves and converted waves in staggered-grid FDM, seismic records are extracted from seven receivers (R1-R7, at depths of 980 m) at offsets of -1480, -960, -440, 80, 490, 1110, and 1640 m, and compared with results obtained from SEM (see Fig. 6). The SEM results are derived using the open-source software SPECFEM2D (Komatitsch and Vilotte, 1998; Komatitsch and Tromp, 1999; Komatitsch et al., 2000a, 2016; Komatitsch and Martin, 2007; Tromp et al., 2008). Through single-trace seismic record comparisons, it becomes evident that the simulated amplitudes and phases of seismic waves closely match those obtained from SEM, thus validating the accuracy of our method.

Next, we utilize Model 2 for numerical simulation, which allows for a more effective observation of the Leaky Rayleigh wave mode (Zhu and Popovics, 2006) and Scholte wave propagating along the interface. Model 2 has dimensions of 2000 m \times 2000 m, with a grid size of 501 \times 501 and a grid spacing of 4 m. In this

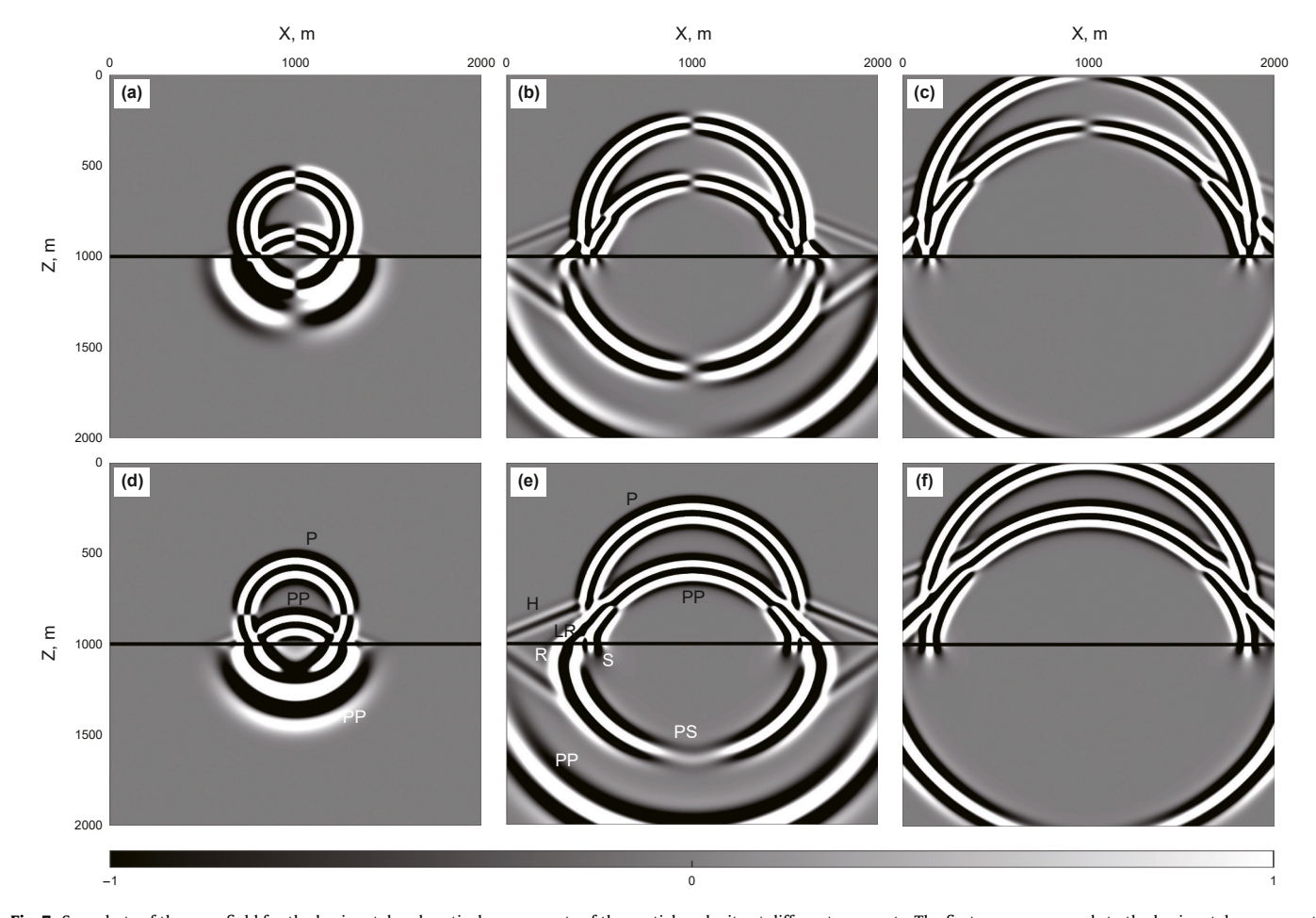


Fig. 7. Snapshots of the wavefield for the horizontal and vertical components of the particle velocity at different moments. The first row corresponds to the horizontal component of the particle velocity and the second row to the vertical component of the particle velocity. Subplots (a), (b) and (c) correspond to wavefield snapshots at t = 0.30 s, t = 0.50 s and t = 0.70 s, respectively. P represents direct acoustic waves, PP represents reflected P and transmitted P waves, PS represents converted S waves, H represents the head wave associated with the transmitted P wave, S represents Scholte waves, R represents Rayleigh waves, and LR represents the Leaky mode Rayleigh waves.

model, the P-wave velocity in the solid portion is 4000 m/s, the Swave velocity is 2300 m/s, and the density is 2400 kg/m³. The parameters of the fluid portion are consistent with Model 1. A pressure source is located within the fluid at a depth of 840 m, positioned 160 m above the fluid-solid interface. The source wavelet is a Ricker wavelet with a dominant frequency of 15 Hz. recorded for 1 s with a time step of 0.4 ms. Horizontal arrays of receivers are positioned 8 m above the fluid-solid interface, with a spacing of 8 m between receivers. The horizontal and vertical components of the wavefield snapshots at different time steps are depicted in Fig. 7. These snapshots illustrate the accurate simulation of wave propagation phenomena at the fluid-solid interface, encompassing acoustic waves in the fluid region, transmitted Pwaves in the solid region, P-S converted waves, Leaky Rayleigh waves, and Scholte waves propagating along the fluid-solid interface. Similarly to Model 1, seismic recordings from seven receivers (R1-R7, at depths of 992 m) at offsets of -732 m, -460 m, -188 m,84 m, 356 m, 628 m, and 900 m are extracted and compared with results obtained using the SEM method. As illustrated in Fig. 8, a close agreement between the two methods is observed, underscoring the feasibility of implicitly expressing fluid-solid boundary conditions in staggered-grid FDM and the effectiveness of simulating seismic wave propagation in fluid-solid coupled media.

3.2. Case 2: an irregular fluid-solid interface model

In this section, we demonstrate the effectiveness of the derived expression for the irregular fluid-solid interface in staggered-grid FDM through numerical experiments. As depicted in Fig. 9, we construct a solid-fluid coupled model featuring an irregular interface. The model dimensions are 3840 m \times 2880 m, discretized into 1281 \times 961 grids. The lower solid region exhibits a P-wave

velocity of 3500 m/s, S-wave velocity of 1963 m/s, and density of 2500 kg/m³, while the upper fluid region has a P-wave velocity of 1500 m/s and density of 1000 kg/m³. A seismic source is positioned in the fluid region, represented by a pressure source excited at a depth of 1140 m (as indicated by the red star in Fig. 9). The source time function is a Ricker wavelet with a dominant frequency of 17 Hz, recorded for 1.6 s with a time step of 0.4 ms. Fig. 10(a)–(c) and Fig. 11(a)–(c) respectively illustrate the horizontal and vertical components of wavefield snapshots at different times (t = 0.48 s, t = 0.90 s, and t = 1.28 s). These snapshots clearly depict transmitted P-waves and P-S waves in the solid region,

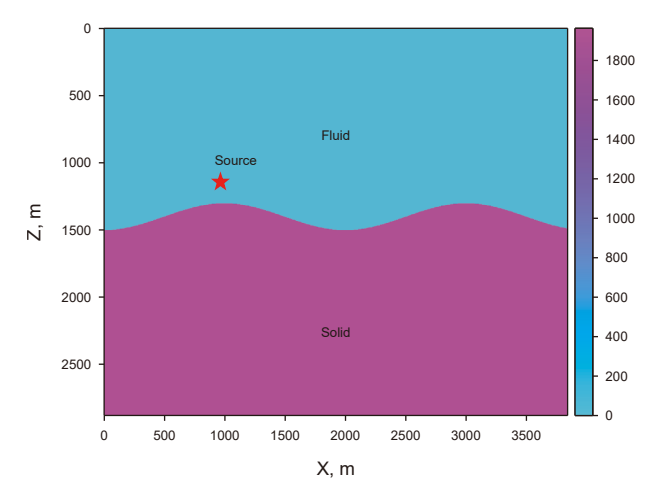


Fig. 9. Schematic diagram of the fluid-solid coupled model at the irregular interface, where the red stars represent the location of the source.

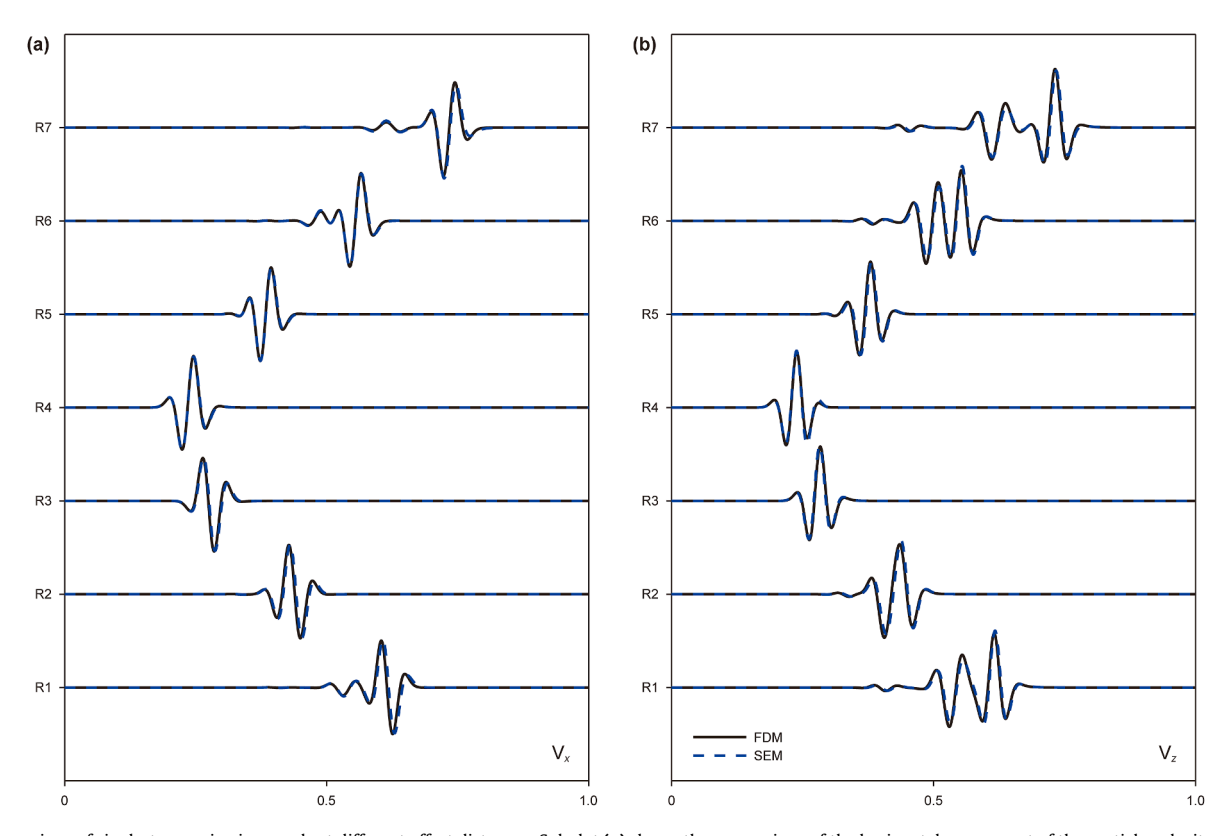


Fig. 8. Comparison of single-trace seismic records at different offset distances. Subplot (a) shows the comparison of the horizontal component of the particle velocity and subplot (b) shows the vertical component of the particle velocity.

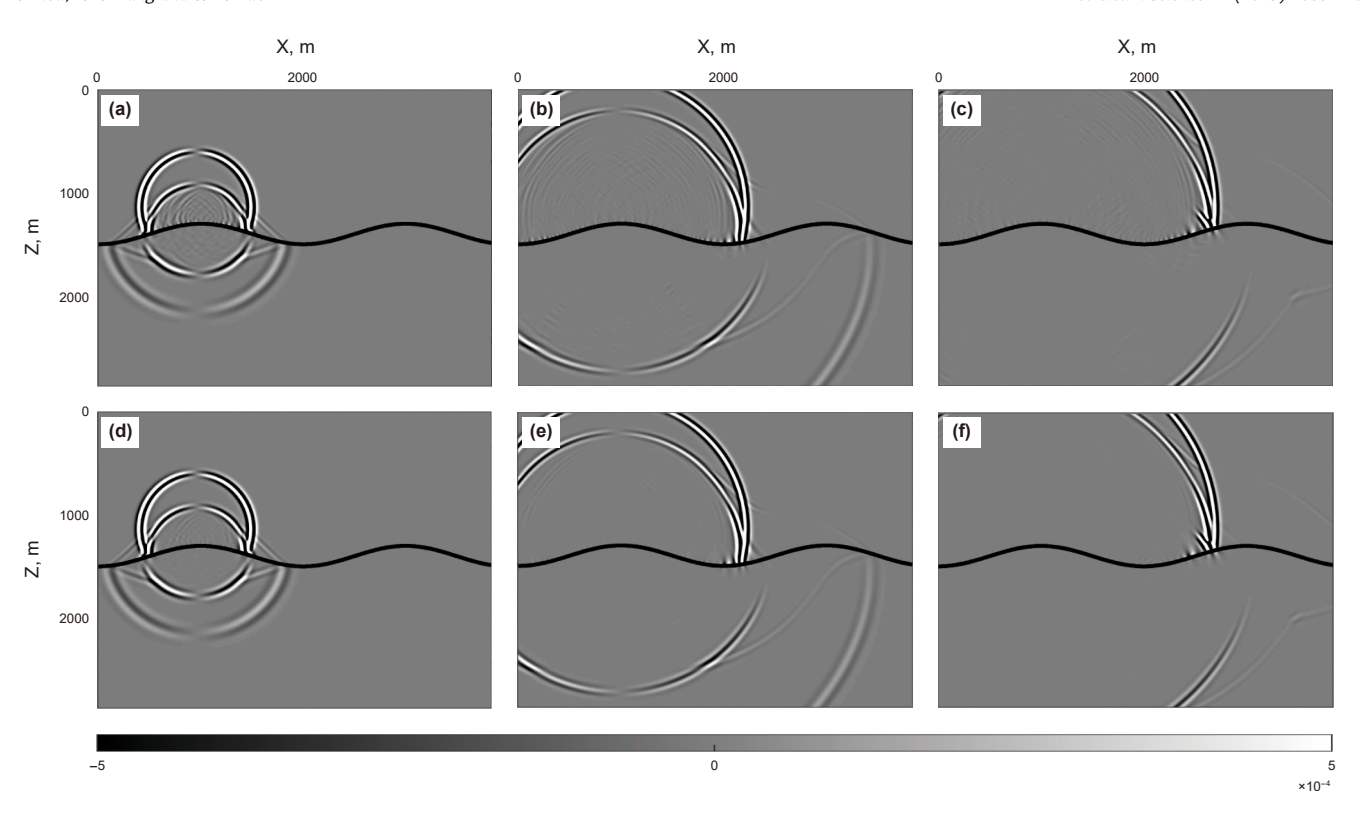


Fig. 10. Snapshots of the wavefield at different moments of the horizontal component of the particle velocity in the irregular fluid-solid interface model, subplots (a), (b) and (c) show the simulation results without the use of the superposition method to discretize the irregular interface; subplots (d), (e) and (f) show the simulation results after the use of the superposition method to discretize the irregular interface.

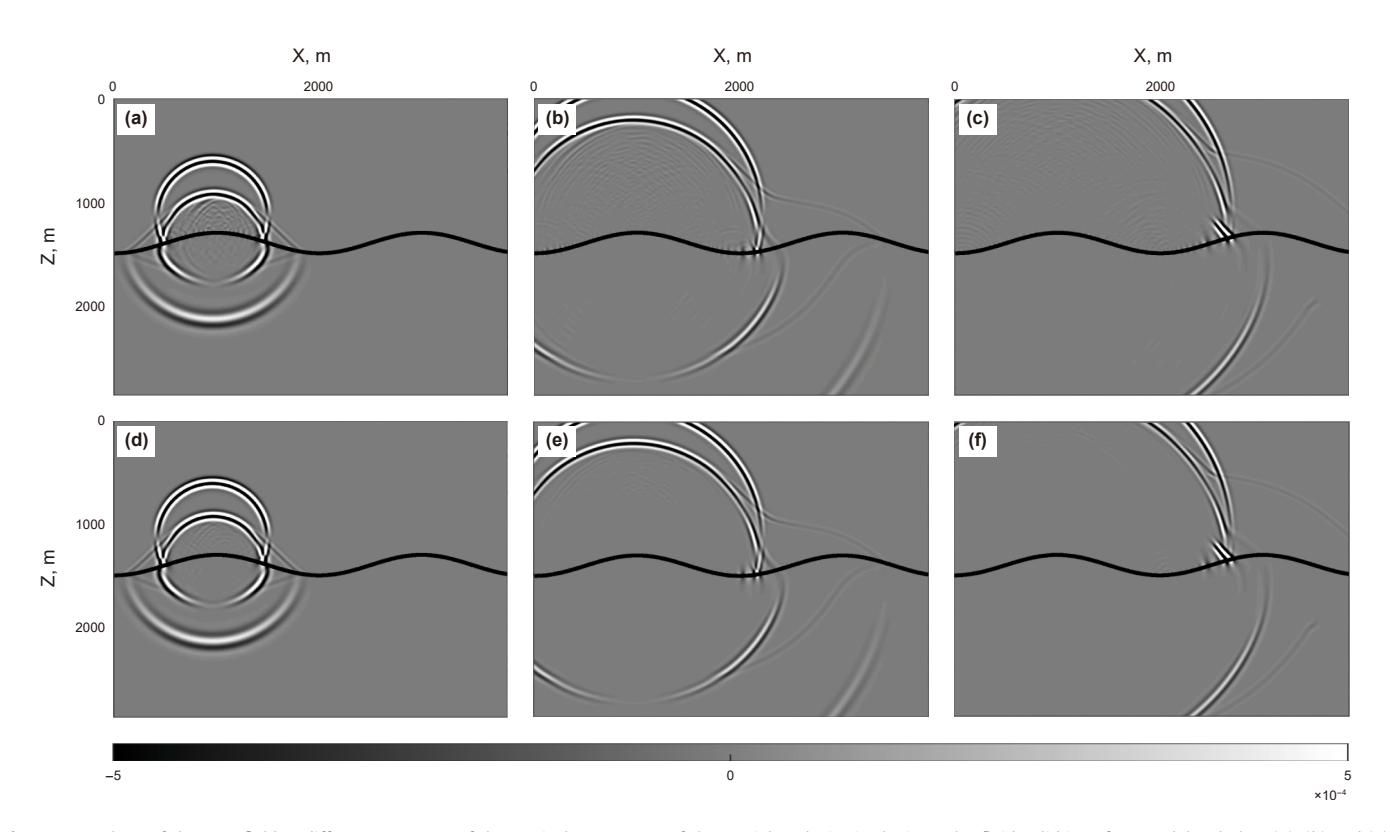


Fig. 11. Snapshots of the wavefield at different moments of the vertical component of the particle velocity in the irregular fluid-solid interface model, subplots (a), (b) and (c) show the simulation results without the use of the superposition method to discretize the irregular interface; subplots (d), (e) and (f) show the simulation results after the use of the superposition method to discretize the irregular interface.

acoustic waves in the fluid region, and the propagation of Scholte waves and leaky Rayleigh waves along the interface. This observation confirms the effectiveness of the proposed expression for the irregular fluid-solid interface. However, noticeable diffraction noise is also observed in the fluid region of the wavefield snapshots, stemming from scattering at the turning points of grid cells approximating irregular surfaces using staircase functions. Fig. 12 presents the horizontal and vertical components of particle velocity single-shot records for SEM and FDM numerical simulations of the fluid-solid coupled model. The first row represents horizontal particle velocity components, while the second row represents vertical components. Fig. 12(a) and (d) depict the results of SEM, whereas Fig. 12(b) and (e) illustrate the results of the proposed FDM. From the single-shot records, it is evident that, aside from the pronounced staircase diffraction noise, the results obtained by the proposed FDM closely resemble those of SEM.

To mitigate staircase diffraction noise, we employ the superposition method to discretize the irregular fluid-solid interface. Before conducting numerical experiments, we needed to determine a suitable value of N to set different thresholds for the staircase discretization of the irregular interface. If N is too large, it

will increase the computational cost, and if it is too small, it may not effectively suppress the staircase diffractions. To determine the appropriate value of N, we compared the results calculated by the proposed method with those calculated by the SPECFEM2D software package and calculated the L₂ norm misfits. Fig. 13 shows the relationship between different values of N and L₂ norm misfits, and it can be observed that when N < 6, the error decreases gradually with the increase of N. When N > 6, the magnitude of the error reduction becomes smaller with the increase of N. Considering both computational cost and the L₂ norm misfits, we choose N = 6 for the following numerical tests. The second rows in Figs. 10 and 11 illustrate the simulation results obtained after discretizing the irregular interface using the superposition method. Comparing these results with those obtained in the first row without using the superposition method, we can clearly observe effective suppression of staircase diffraction noise. Fig. 12(c) and (f) present singleshot records obtained after discretizing the irregular interface using the superposition method, showcasing the suppression effect on staircase diffraction noise. To further illustrate the effectiveness of the superposition method, Fig. 12(g) compares a seismic record at an offset of 60 m. The blue trace represents the

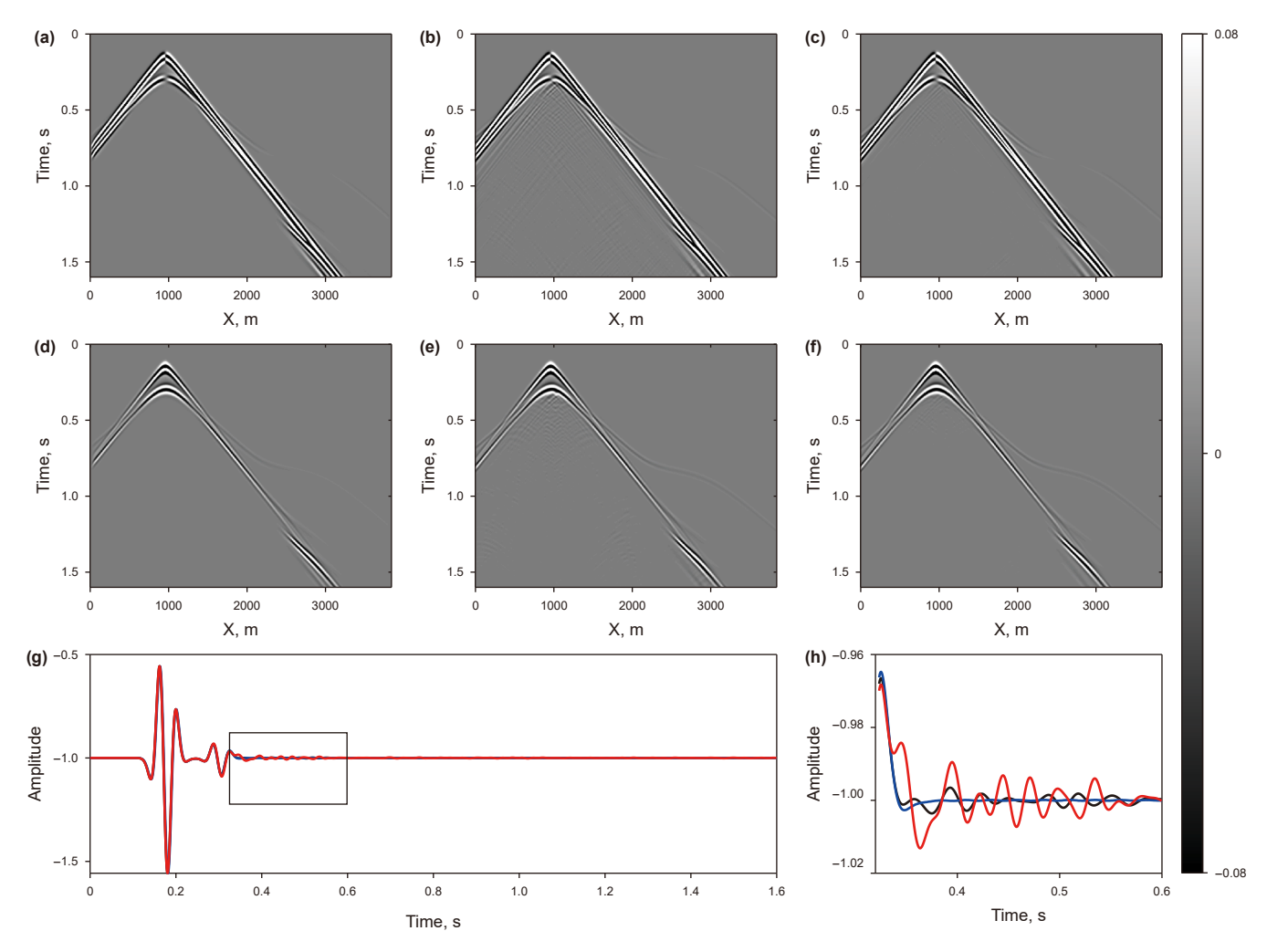


Fig. 12. Single-shot records of particle velocities in the irregular fluid-solid interface model and single-trace comparison, subplots (a), (b) and (c) are single-shot records of the horizontal component of particle velocities obtained by the SEM, the FDM without the superposition method and the FDM with the superposition method; subplots (d), (e) and (f) are single-shot records of the vertical component of particle velocities obtained by the SEM, the FDM without the superposition method and the FDM with the superposition method; subplot (g) is a single-trace comparison of the three results at an offset distance of 60 m. Subplot (h) is an enlarged version of the waveform comparison within the black box in subplot (g). The blue line is the result of the SEM, the black and red lines correspond to the results obtained with the FDM with and without the superposition method, respectively.

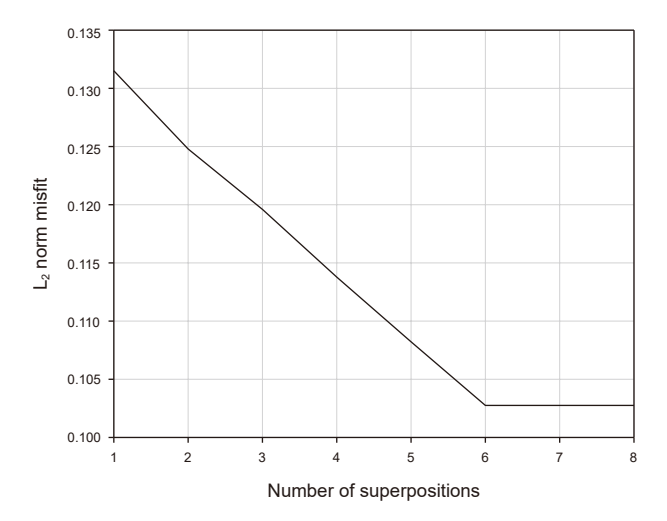


Fig. 13. L₂ norm misfits corresponding to different numbers of superpositions.

SEM result, while the black and red traces correspond to the FDM results obtained with and without the superposition method, respectively. It is evident that the staircase diffraction noise in the results obtained after superposition-based discretization of the irregular interface is effectively suppressed, thereby demonstrating the effectiveness of our superposition method in mitigating staircase diffraction noise. Finally, to verify the accuracy of the proposed method in numerically simulating irregular fluid-solid interfaces, we compare single-trace records from seven receivers located at offsets of -237, -60, 240, 663, 840, 1224, and

1575 m with SEM, as shown in Fig. 14. From Fig. 14, we observe good agreement between both horizontal and vertical particle velocity components and the results obtained from SEM, thereby confirming the accuracy of the proposed FDM in numerical simulation when dealing with irregular fluid-solid interfaces. In the comparison, we further include the treatment of harmonic averaging of the shear modulus. We can see that the harmonic averaging treatment does not fit the reference results well at far offset distances (e.g., the vertical component of the R7 receiver) compared to the proposed method.

3.3. Case 3: a layered fluid-solid coupled model

Finally, based on the irregular fluid-solid interface double-layer model, we establish a multi-layer model. The schematic diagram of the model and the P-wave velocity and density for each layer are illustrated in Fig. 15, where the units for velocity are m/s and for density are kg/m³. Except for the water layer, the S-wave velocity of the solid layer can be determined from a Poisson's ratio of 0.25. The pressure source is positioned within the fluid at a depth of 540 m, as indicated by the red star in Fig. 15. The source wavelet is a 13 Hz Ricker wavelet, with a recording time of 2 s and a time step of 0.2 ms. The comparison of the recorded single-shot records is depicted in Fig. 16, where the three columns from left to right represent the results of SEM, FDM without using the superposition method, and FDM using the superposition method, respectively. From the single-shot records, the presence of inter-layer reflection waves is clearly observed. Additionally, the existence of staircase noise is evident in (b) and (e) of Fig. 16, obscuring the reflection wave signals. However, after employing the superposition method

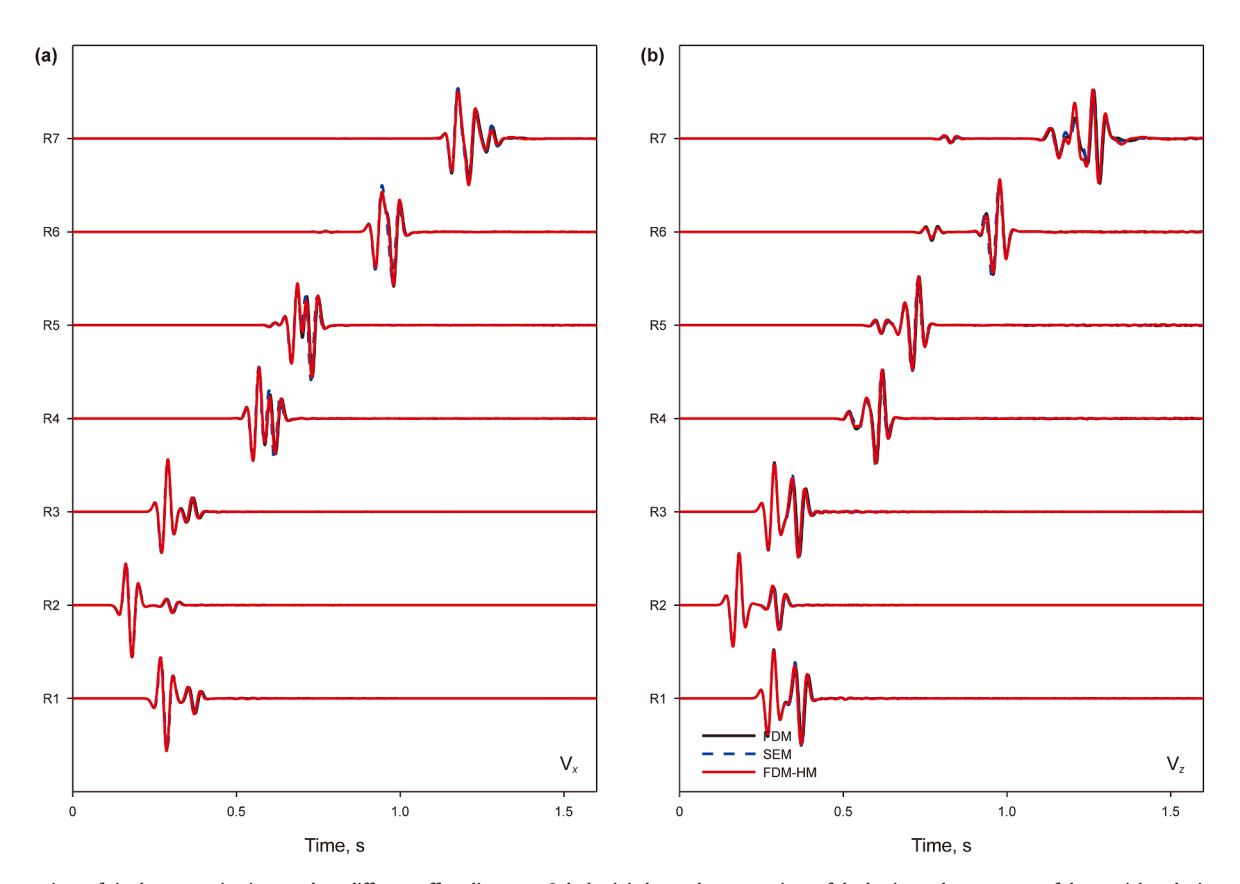


Fig. 14. Comparison of single-trace seismic records at different offset distances. Subplot (a) shows the comparison of the horizontal component of the particle velocity and subplot (b) shows the vertical component of the particle velocity. FDM-HM refers here to the result of implicitly processing the boundary conditions using harmonic averaging of the shear modulus.

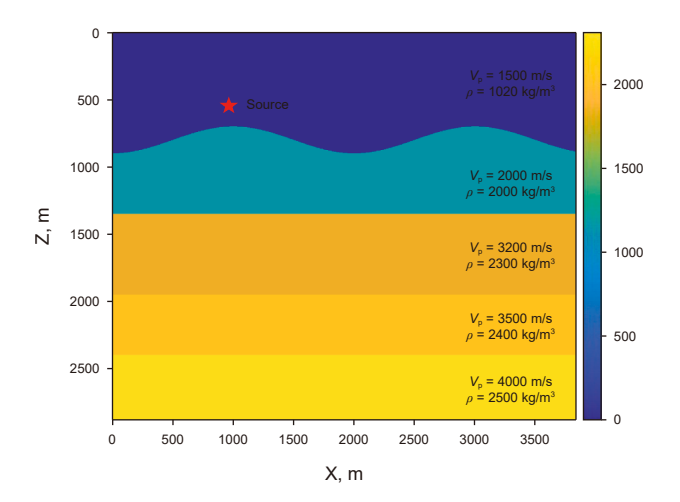


Fig. 15. Layered fluid-solid coupled model, where the red stars represent the location of the source.

for irregular interface discretization, the staircase diffraction noise is effectively suppressed, and its presence is no longer observed in the reflection wave portion. To further validate the accuracy of the proposed method, single-trace records at different offsets were compared with SEM, as shown in Fig. 17, for both the horizontal and vertical components of particle velocity. From the comparison results, it can be observed that the results of FDM are in good agreement with SEM, further demonstrating the effectiveness and accuracy of our method in modeling irregular seabed layer models.

4. Discussion

4.1. Computational costs and memory requirements

When utilizing the superposition method to discretize irregular fluid-solid interfaces, six different discretizations are necessary to effectively suppress staircase diffraction noise. To illustrate the computational cost issue, we conducted numerical simulations using a simplified model, as shown in Fig. 18. The model has dimensions of 2000 m × 1000 m, discretized into two cases: 501×251 grids and 1001×501 grids, corresponding to grid spacings of 4 m and 2 m, respectively. In the solid portion, the Pwave velocity is 2700 m/s, the S-wave velocity is 1400 m/s, and the density is 1200 kg/m³. In the fluid portion, the P-wave velocity is 1500 m/s, and the density is 1000 kg/m³. A pressure source is located at the red star in Fig. 18. Fig. 19 illustrates the recorded single-shot records, with the first row indicating the horizontal component of particle velocity and the second row indicating the vertical components. From left to right, the three columns represent grid spacings of h = 2 m, h = 4 m, and h = 4 m using the superposition method for discretization, where h is the grid spacing. From Fig. 19, it is evident that using a grid spacing of h = 4 m for numerical simulation results in noticeable staircase diffraction noise (Fig. 19(b) and (e)). When the grid is refined to h = 2 m, the staircase diffraction noise is effectively suppressed (Fig. 19(a) and (d)). Similarly, employing the superposition method for discretization with h = 4 m results in effective suppression of staircase diffraction noise (Fig. 19(c) and (f)). Furthermore, a comparison is made between the results obtained using the superposition method for discretization and those obtained with h = 2 m. The comparison of single-shot records is shown in Fig. 20.

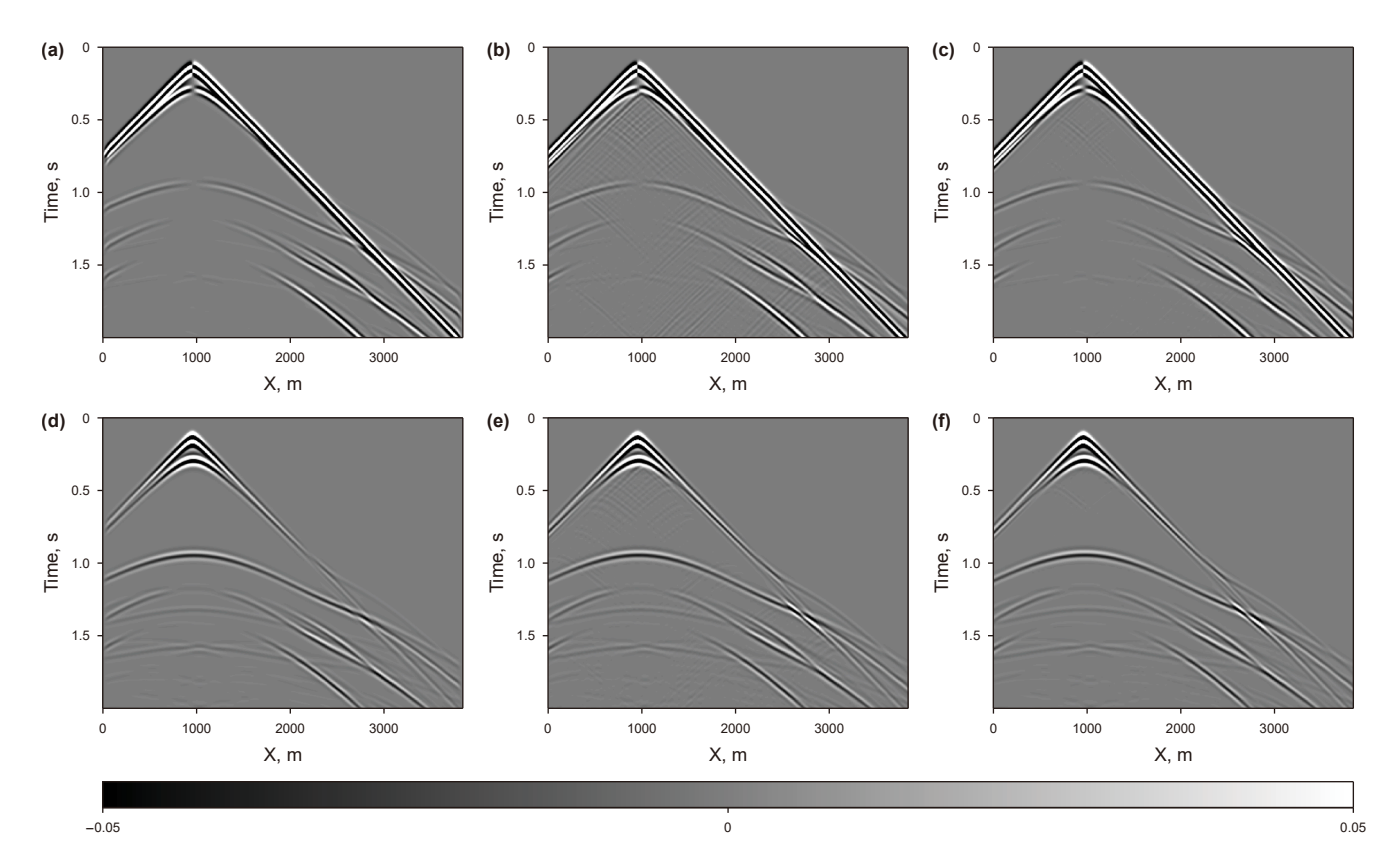


Fig. 16. Single-shot records of particle vibration velocities in the layered fluid-solid coupled model, subplots (a), (b) and (c) are single-shot records of the horizontal component of particle velocities obtained by the SEM, the FDM without the superposition method and the FDM with the superposition method; subplots (d), (e) and (f) are single-shot records of the vertical component of particle velocities obtained by the SEM, the FDM without the superposition method and the FDM with the superposition method.

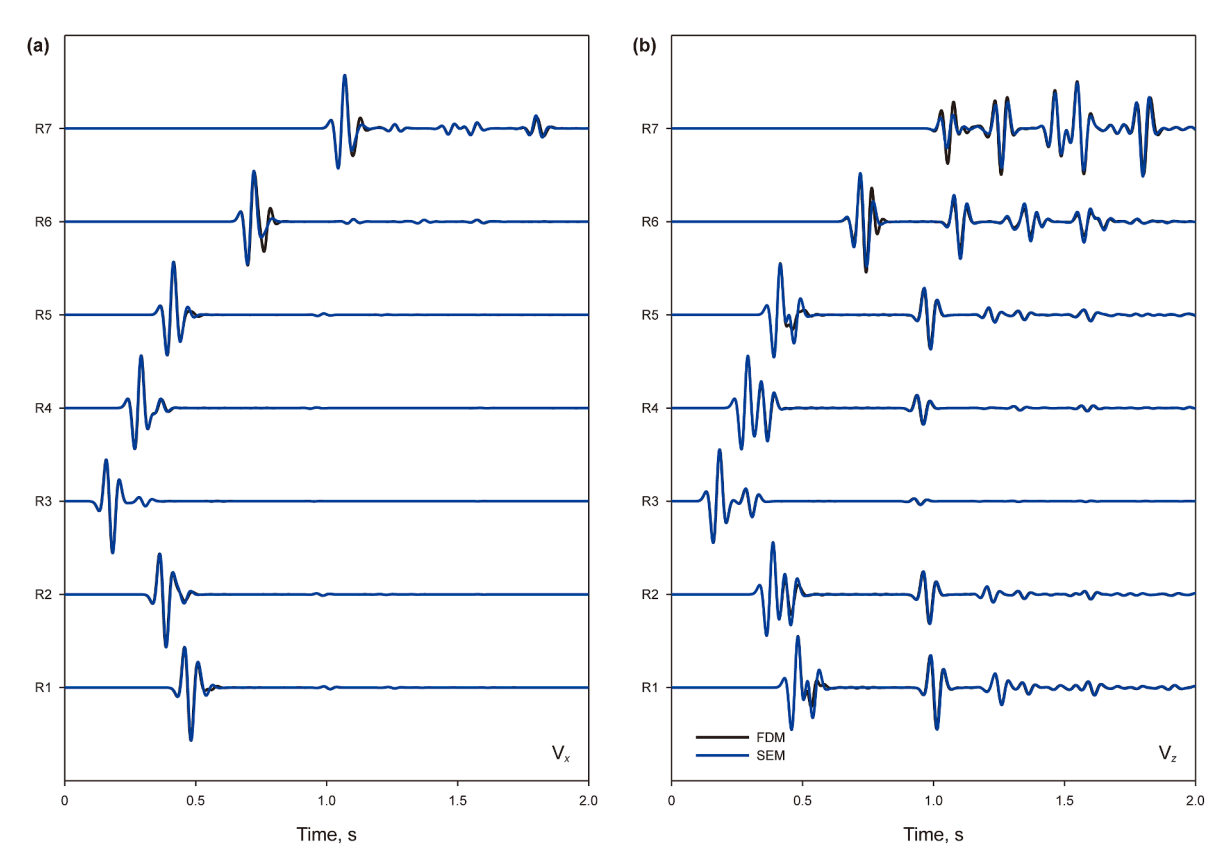


Fig. 17. Comparison of single-trace seismic records at different offset distances. Subplot (a) shows the comparison of the horizontal component of the particle velocity and subplot (b) shows the vertical component of the particle velocity.

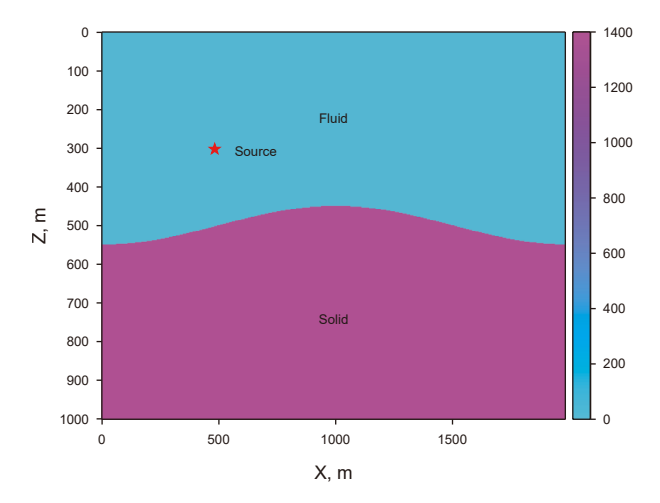


Fig. 18. Schematic diagram of the simple model, where the red star shows the location of the source.

The comparison demonstrates good agreement between the two, indicating that using a grid spacing of h=4 m in conjunction with the superposition method for discretization achieves precision and reduces staircase diffraction noise intensity comparable to that obtained with h=2 m. The calculations were executed on an AMD Ryzen 9 5950X processor. The computation time for discretization using a grid spacing of h=4 m in conjunction with the

superposition method was 406 s, while the computation time for a grid spacing of h = 2 m was 552 s. Thus, the proposed discretization method using the superposition method reduces computation time compared to conventional grid spacing. The grid spacing of h = 2 m necessitates twice the sampling in each Cartesian direction compared to h = 4 m. Additionally, for smaller grid spacings, the time step must be reduced to meet stability criteria. Therefore, as the grid spacing decreases from h = 2 m to h = 4 m, the computational cost reduces by 8 times. Considering six superposition iterations, the final computation cost using the superposition method for discretization with a grid spacing of h = 4 m should ideally be 3/4 of the computation cost with h=2 m. The ratio of computation times in our calculations is close to 3/4, further confirming our inference. If extended to three-dimensional numerical simulations, the ideal computation cost using the superposition method for discretization should be 3/8 of the computation cost with conventional grid spacing. From the above comparison, it can be observed that when employing the superposition method for discretization, the computation cost is reduced compared to spatial sampling strategies that effectively suppress staircase diffraction noise.

Furthermore, when employing smaller grid spacing for numerical simulations, all stresses, velocities, and other parameters at every grid point must be stored in memory simultaneously, leading to a significant demand for memory. Once memory requirements cannot be met, it becomes challenging to obtain high-resolution numerical simulation results. The method we propose involves using larger grid spacing for

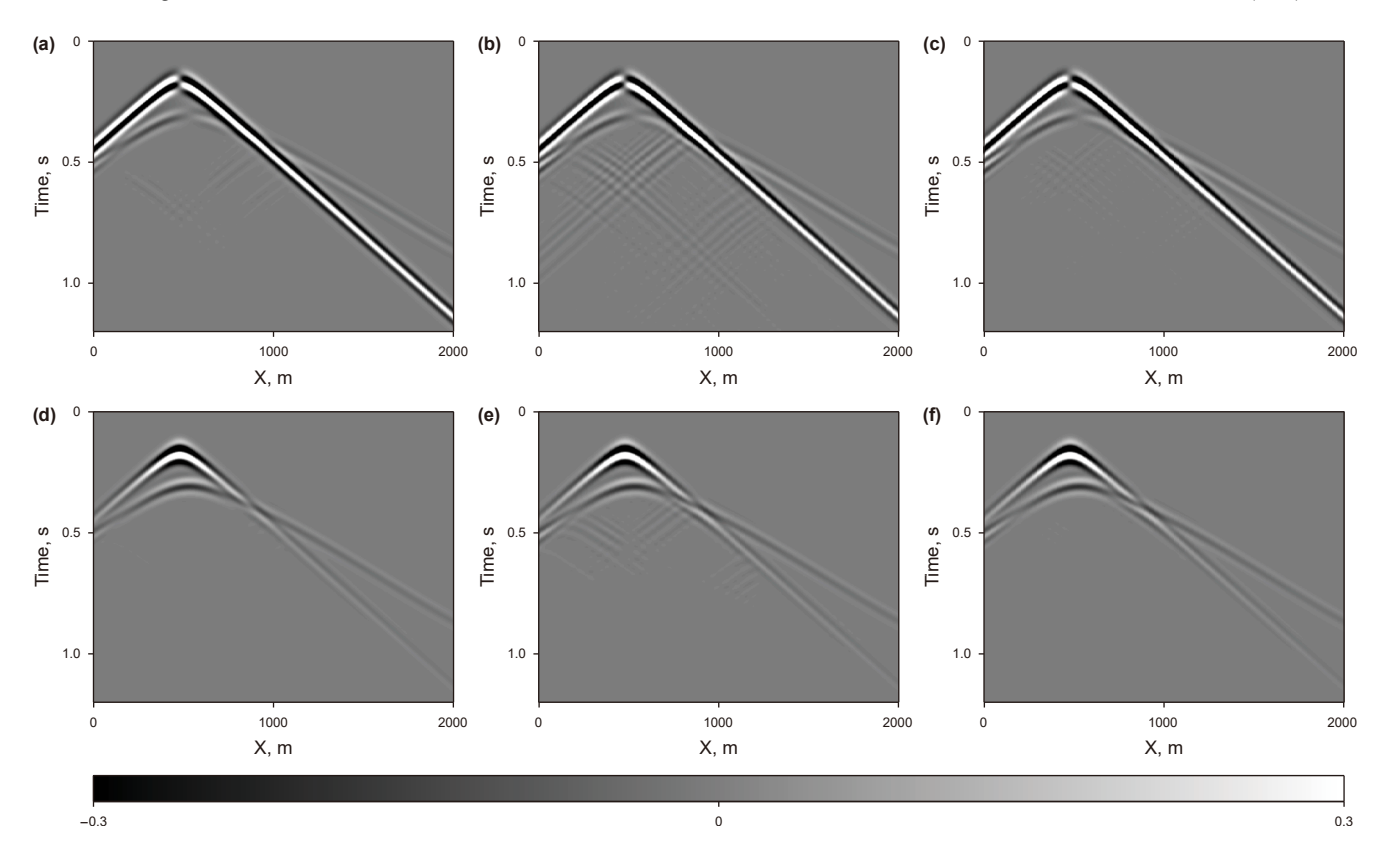


Fig. 19. (a), (b) and (c) are single-shot records of the horizontal component of the particle velocity for h = 2 m, h = 4 m and h = 4 (using the superposition method of discretization), and (d), (e) and (f) are single-shot records of the vertical component of the particle velocity for h = 2 m, h = 4 m and h = 4 m (using the superposition method of discretization) in the simple irregular fluid-solid interface model.

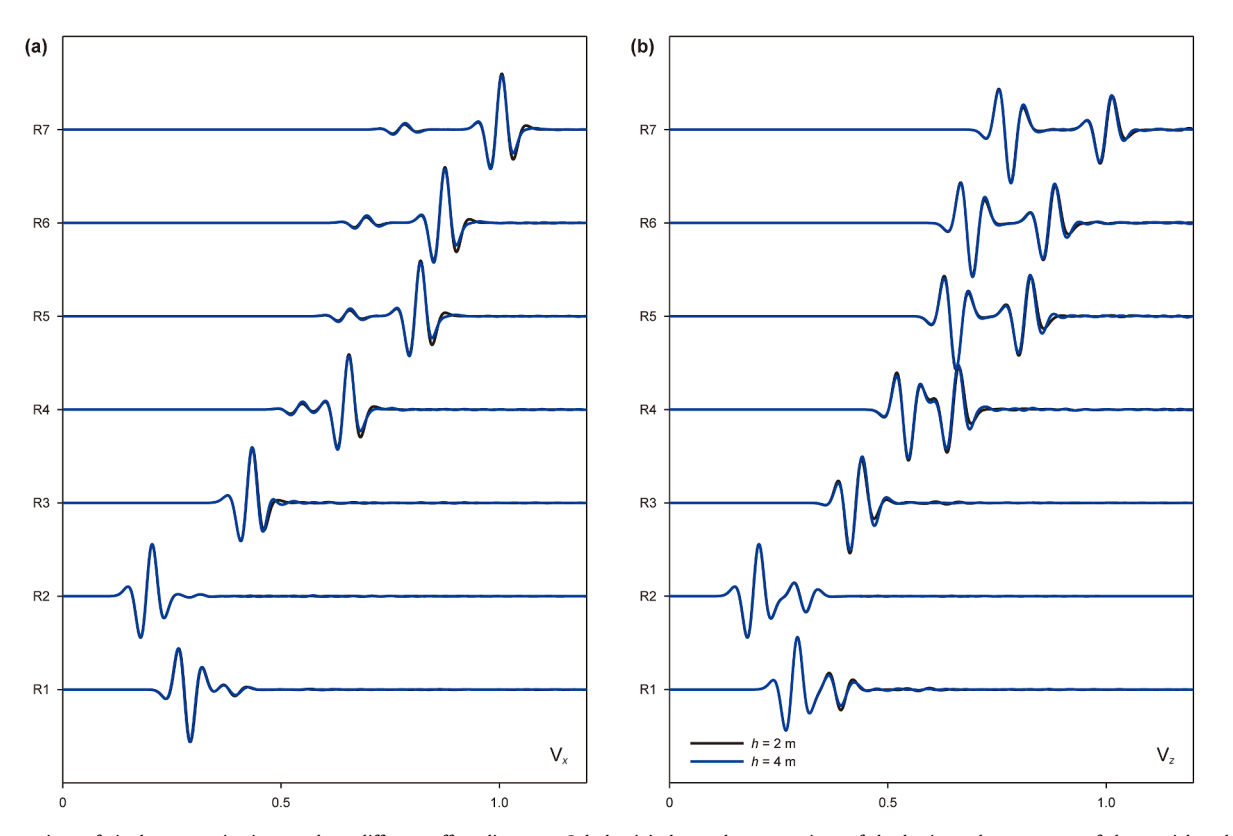


Fig. 20. Comparison of single-trace seismic records at different offset distances. Subplot (a) shows the comparison of the horizontal component of the particle velocity and subplot (b) shows the vertical component of the particle velocity.

multiple independent numerical simulations. With this approach, the larger memory requirements are distributed among the individual numerical simulations, making it easier to meet memory demands. This distributed memory usage strategy facilitates high-resolution simulations without exceeding memory constraints.

4.2. Code portability and expandability

The proposed method involves straightforward modifications of model parameters at the interface. This simplicity makes it easy to adapt for conventional Cartesian staggered-grid FDM schemes and commonly used GPU parallel computing systems in the oil and gas industry. Moreover, the method can be readily extended to other types of media, including anisotropic media, viscoelastic media, and more.

5. Conclusion

To address the challenges of untreated boundary conditions and staircase diffraction noise in irregular interfaces when employing the first-order velocity-stress staggered-grid FDM for fluid-solid coupled medium numerical simulation, this paper proposes two solutions:

- (1) Implicit Boundary Condition Expression: Leveraging average medium theory and fluid-solid boundary conditions, the paper deduces constitutive and density relationships at the fluid-solid boundary. By modifying interface parameters based on these relationships, explicit fluid-solid boundary conditions are implicitly incorporated into numerical simulations.
- (2) Superposition-based Interface Discretization: Utilizing the superposition method, the interface undergoes multiple discretizations by employing different thresholds. Numerical simulations are conducted for each discretized interface model, and the final results are obtained through superposition.

Numerical experiments demonstrate that the proposed method yields simulation results in good agreement with the SEM for both horizontal and irregular interfaces. Furthermore,

employing the superposition method for fluid-solid interface discretization effectively suppresses staircase diffraction noise without necessitating grid refinement. Despite conducting multiple simulations for the same model, the computational cost remains low compared to grid refinement, and memory requirements are effectively reduced.

CRediT authorship contribution statement

Xu-Hui Zhou: Writing – original draft, Software, Methodology, Investigation, Conceptualization. **Yi-Yuan Wang:** Data curation, Software, Supervision, Validation, Visualization. **Shou-Dong Huo:** Writing – review & editing, Supervision, Funding acquisition.

Declaration of competing interest

The authors declare that they have no known competing financial interests or personal relationships that could have appeared to influence the work reported in this paper.

Acknowledgements

This work was supported by the National Natural Science Foundation of China (Nos. 42404134, U24B2031, 42174160), the China Postdoctoral Science Foundation (No. 2024M753204), and the National Key R & D Program of China (Nos. 2021YFA0716901, 2022YFB3904601).

Appendix

In marine seismic exploration, geophones are typically placed on the seafloor or via streamers below the sea surface. It's uncommon to place them in the rock or weathered layer beneath the seafloor. Yet, to verify the feasibility and accuracy of our method, we resimulated the four models in the "Numerical experiment" part, placing geophones at the vertical mirror position relative to the original ones. We then compared the results with those from the SEM method. The comparison results for Model 1, Model 2, the simple irregular-surface model, and the layered irregular-surface model are in Figs. A1–A4. The results indicate that our method can also fit the SEM results well when signals are received in the solid.

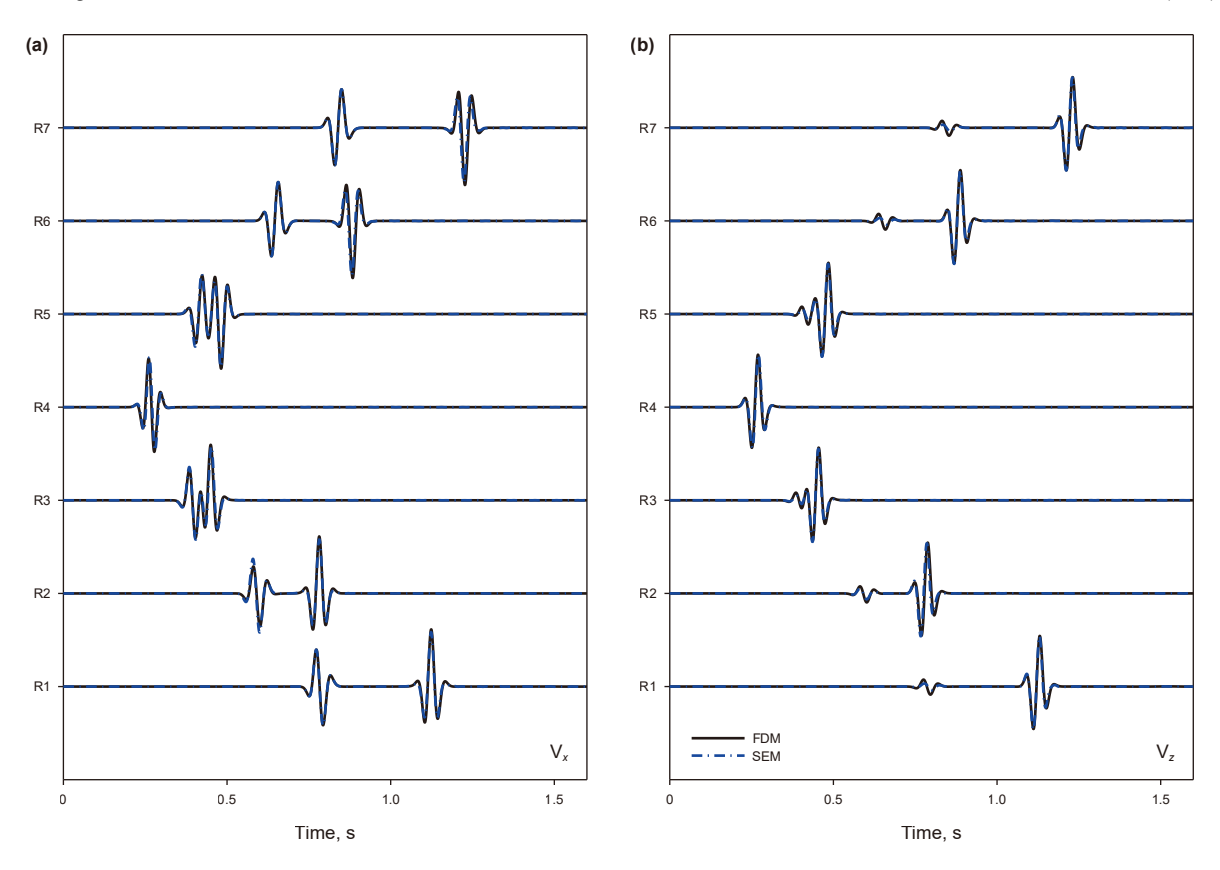


Fig. A1. Model 1: comparison of single-trace seismic records at different offset distances. Subplot (a) shows the comparison of the horizontal component of the particle velocity and subplot (b) shows the vertical component of the particle velocity.

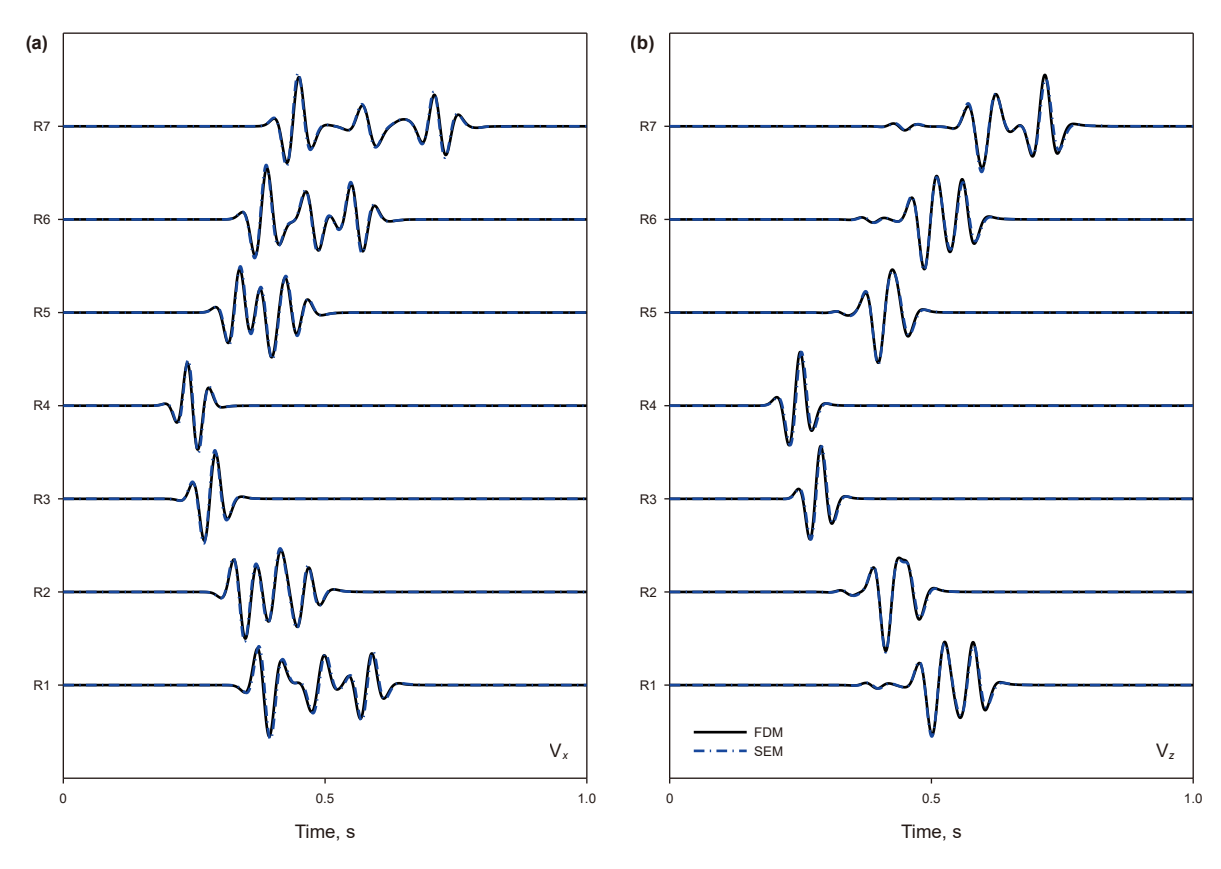


Fig. A2. Model 2: comparison of single-trace seismic records at different offset distances. Subplot (a) shows the comparison of the horizontal component of the particle velocity and subplot (b) shows the vertical component of the particle velocity.

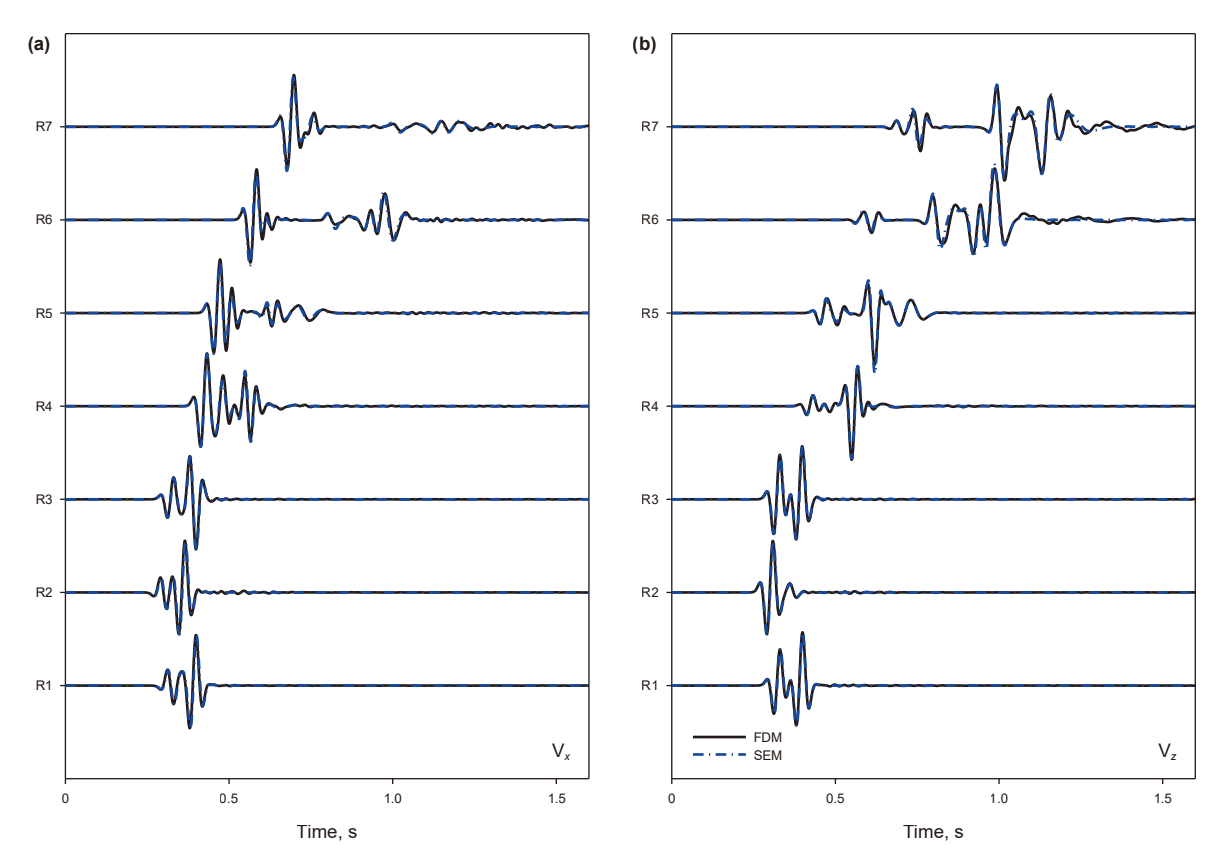


Fig. A3. The simple irregular-surface model: comparison of single-trace seismic records at different offset distances. Subplot (a) shows the comparison of the horizontal component of the particle velocity and subplot (b) shows the vertical component of the particle velocity.

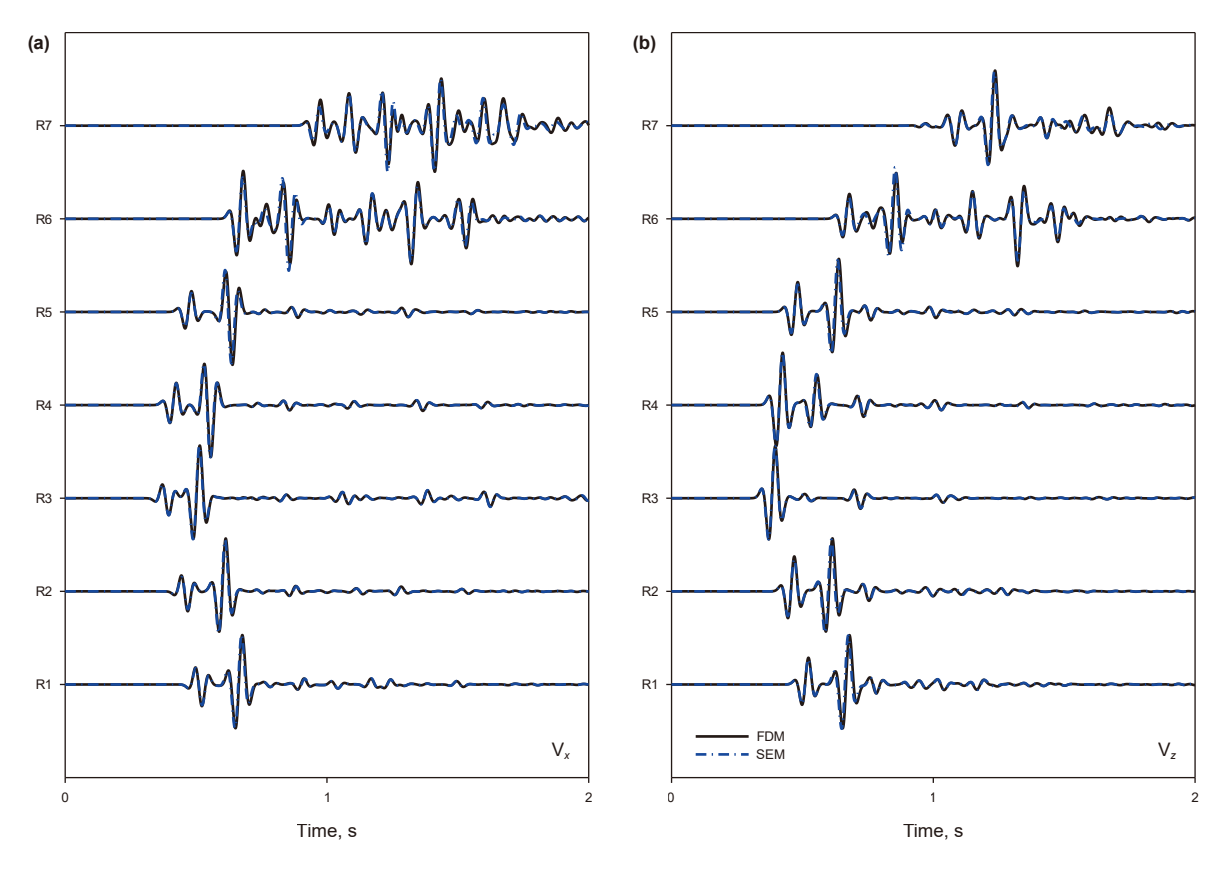


Fig. A4. The layered irregular-surface model: comparison of single-trace seismic records at different offset distances. Subplot (a) shows the comparison of the horizontal component of the particle velocity and subplot (b) shows the vertical component of the particle velocity.

References

- Agudo, O.C., da Silva, N.V., Stronge, G., et al., 2020. Mitigating elastic effects in marine 3-D full-waveform inversion. Geophys. J. Int. 220 (3), 2089–2104. https://doi.org/10.1093/gii/ggz569.
- Alterman, Z., Karal, Jr F., 1968. Propagation of elastic waves in layered media by finite difference methods. Bull. Seismol. Soc. Am. 58 (1), 367–398. https://doi. org/10.1785/BSSA0580010367.
- Antonietti, P.F., Bonaldi, F., Mazzieri, I., 2020. Simulation of three-dimensional elastoacoustic wave propagation based on a Discontinuous Galerkin spectral element method. Int. J. Numer. Methods Eng. 121 (10), 2206–2226. https://doi.org/10.1002/nme.6305.
- Cao, J., Brossier, R., Gorszczyk, A., et al., 2022. 3-D multiparameter full-waveform inversion for ocean-bottom seismic data using an efficient fluid-solid coupled spectral-element solver. Geophys. J. Int. 229 (1), 671–703. https://doi.org/10.1093/gji/ggab484.
- Cao, J., Chen, J.B., 2018. A parameter-modified method for implementing surface topography in elastic-wave finite-difference modeling. Geophysics 83 (6), T313–T332. https://doi.org/10.1190/geo2018-0098.1.
- Cao, J., Chen, J.B., Dai, M.X., 2018. An adaptive free-surface expression for three-dimensional finite-difference frequency-domain modelling of elastic wave. Geophys. Prospect. 66 (4), 707–725. https://doi.org/10.1111/1365-2478.12618.
- Carcione, J.M., Helle, H.B., 2004. The physics and simulation of wave propagation at the ocean bottom. Geophysics 69 (3), 825–839. https://doi.org/10.1190/1.1759469.
- Chen, H., Chen, K., Wang, L., et al., 2024. An efficient immersed free surface boundary method for 3-D scalar seismic waves finite-difference modeling in presence of topography. IEEE Trans. Geosci. Rem. Sens. 62, 1–12. https://doi. org/10.1109/TGRS.2024.3385239.
- De Basabe, J.D., Sen, M.K., 2015. A comparison of finite-difference and spectralelement methods for elastic wave propagation in media with a fluid-solid interface. Geophys. J. Int. 200 (1), 278–298. https://doi.org/10.1093/gji/ggu389.
- de la Puente, J., Ferrer, M., Hanzich, M., et al., 2014. Mimetic seismic wave modeling including topography on deformed staggered grids. Geophysics 79 (3), T125-T141. https://doi.org/10.1190/geo2013-0371.1.
- Drainville, R.A., Curiel, L., Pichardo, S., 2019. Superposition method for modelling boundaries between media in viscoelastic finite difference time domain simulations. J. Acoust. Soc. Am. 146 (6), 4382–4401. https://doi.org/10.1121/ 1.5139.221.
- Graves, R.W., 1996. Simulating seismic wave propagation in 3D elastic media using staggered-grid finite differences. Bull. Seismol. Soc. Am. 86 (4), 1091–1106. https://doi.org/10.1785/BSSA0860041091.
- Guasch, L., Calderon Agudo, O., Tang, M.-X., et al., 2020. Full-waveform inversion imaging of the human brain. npj Digit. Med. 3 (1), 28. https://doi.org/10.1038/s41746-020-0240-8.
- Hou, G.N., Wang, J., Layton, A., 2012. Numerical methods for fluid-structureinteraction a review. Commun. Comput. Phys. 12 (2), 337–377. https://doi.org/10.4208/cicp.291210.290411s.
- Kamath, N., Brossier, R., Metivier, L., et al., 2021. Multiparameter full-waveform inversion of 3D ocean-bottom cable data from the Valhall field. Geophysics 86 (1), B15–B35. https://doi.org/10.1190/geo2019-0705.1.
- Komatitsch, D., Barnes, C., Tromp, J., 2000a. Simulation of anisotropic wave propagation based upon a spectral element method. Geophysics 65 (4), 1251–1260. https://doi.org/10.1190/1.1444816.
- Komatitsch, D., Barnes, C., Tromp, J., 2000b. Wave propagation near a fluid-solid interface: a spectral-element approach. Geophysics 65 (2), 623–631. https:// doi.org/10.1190/1.1444758.
- Komatitsch, D., Martin, R., 2007. An unsplit convolutional perfectly matched layer improved at grazing incidence for the seismic wave equation. Geophysics 72 (5), SM155–SM167. https://doi.org/10.1190/1.2757586.
- Komatitsch, D., Tromp, J., 1999. Introduction to the spectral element method for three-dimensional seismic wave propagation. Geophys. J. Int. 139 (3), 806–822. https://doi.org/10.1046/j.1365-246x.1999.00967.x.
- Komatitsch, D., Vilotte, J.P., 1998. The spectral element method: an efficient tool to simulate the seismic response of 2D and 3D geological structures. Bull. Seismol. Soc. Am. 88 (2), 368–392. https://doi.org/10.1785/BSSA0880020368.
- Komatitsch, D., Xie, Z.N., Bozdag, E., et al., 2016. Anelastic sensitivity kernels with parsimonious storage for adjoint tomography and full waveform inversion. Geophys. J. Int. 206 (3), 1467–1478. https://doi.org/10.1093/gji/ggw224.
- Kristek, J., Moczo, P., Archuleta, R.J., 2002. Efficient methods to simulate planar free surface in the 3D 4th-order staggered-grid finite-difference schemes. Studia Geophys. Geod. 46 (2), 355–381. https://doi.org/10.1023/A:1019866422821.
- Li, H., Qin, S., Liu, H., et al., 2018. Krauklis wave in a fluid filled single fracture: an experimental study. In: Proceedings of Rock Physics and Digital Rock Applications Workshop. Bejing, China.
 Li, Q., Wu, G., Wu, J., et al., 2019. Finite difference seismic forward modeling
- Li, Q., Wu, G., Wu, J., et al., 2019. Finite difference seismic forward modeling method for fluid-solid coupled media with irregular seabed interface. J. Geophys. Eng. 16 (1), 198–214. https://doi.org/10.1093/jge/gxy017.
- Li, X., Yao, G., Niu, F., et al., 2020. An immersed boundary method with iterative symmetric interpolation for irregular surface topography in seismic wavefield modelling. J. Geophys. Eng. 17 (4), 643–660. https://doi.org/10.1093/jge/ gxaa019.

- Liang, C., O'Reilly, O., Dunham, E.M., et al., 2017. Hydraulic fracture diagnostics from Krauklis-wave resonance and tube-wave reflections. Geophysics 82 (3), D171–D186. https://doi.org/10.1190/geo2016-0480.1.
- Liu, Y., Sen, M.K., 2011. Finite-difference modeling with adaptive variable-length spatial operators. Geophysics 76 (4), T79–T89. https://doi.org/10.1190/ 1.3587223.
- Mittet, R., 2002. Free-surface boundary conditions for elastic staggered-grid modeling schemes. Geophysics 67 (5), 1616–1623. https://doi.org/10.1190/
- Moczo, P., Kristek, J., Vavrycuk, V., et al., 2002. 3D heterogeneous staggered-grid finite-difference modeling of seismic motion with volume harmonic and arithmetic averaging of elastic moduli and densities. Bull. Seismol. Soc. Am. 92 (8), 3042–3066. https://doi.org/10.1785/0120010167.
- Petersson, N.A., Sjogreen, B., 2015. Wave propagation in anisotropic elastic materials and curvilinear coordinates using a summation-by-parts finite difference method. J. Comput. Phys. 299 (15), 820–841. https://doi.org/10.1016/j.jcp.2015.07.023.
- Qu, Y.M., Huang, J.P., Li, Z.C., et al., 2017. A hybrid grid method in an auxiliary coordinate system for irregular fluid-solid interface modelling. Geophys. J. Int. 208 (3), 1540–1556. https://doi.org/10.1093/gji/ggw429.
- Robertsson, J.O.A., 1996. A numerical free-surface condition for elastic/viscoelastic finite-difference modeling in the presence of topography. Geophysics 61 (6), 1921–1934. https://doi.org/10.1190/1.1444107.
- Soares, D., 2008. Numerical modelling of acoustic-elastodynamic coupled problems by stabilized boundary element techniques. Comput. Mech. 42 (6), 787–802. https://doi.org/10.1007/s00466-008-0282-2.
- Soares, D., Mansur, W.J., 2006. Dynamic analysis of fluid-soil-structure interaction problems by the boundary element method. J. Comput. Phys. 219 (2), 498–512. https://doi.org/10.1016/j.jcp.2006.04.006.
- Sun, W.T., Yang, H.Z., 2003. Elastic wavefield calculation for heterogeneous anisotropic porous media using the 3-D irregular-grid finite-difference. Acta Mech. Solida Sin. 16 (4), 283–299. https://doi.org/10.1007/s10338-003-0138-4.
- Sun, Y.C., Zhang, W., Ren, H.X., et al., 2021. 3D seismic-wave modeling with a topographic fluid-solid interface at the sea bottom by the curvilinear-grid finite-difference method. Bull. Seismol. Soc. Am. 111 (5), 2753–2779. https://doi.org/10.1785/0120200363.
- Tessmer, E., Kosloff, D., 1994. 3-D elastic modeling with surface-topography by a Chebyshev spectral method. Geophysics 59 (3), 464–473. https://doi.org/10.1190/1.1443608.
- Tromp, J., Komatitsch, D., Liu, Q.Y., 2008. Spectral-element and adjoint methods in seismology. Commun. Comput. Phys. 3 (1), 1–32.
- van Vossen, R., Robertsson, J.O.A., Chapman, C.H., 2002. Finite-difference modeling of wave propagation in a fluid-solid configuration. Geophysics 67 (2), 618–624. https://doi.org/10.1190/1.1468623.
- Virieux, J., 1986. P-SV wave propagation in heterogeneous media velocity-stress finite-difference method. Geophysics 51 (4), 889–901. https://doi.org/10.1190/
- Xie, C., Qin, Z.-L., Wang, J.-H., et al., 2024a. Full waveform inversion based on hybrid gradient. Pet. Sci. 21 (3), 1660–1670. https://doi.org/10.1016/j. petsci.2024.01.013.
- Xie, C., Wang, J., Song, P., et al., 2024b. Elastic reverse time migration based on first-order velocity-dilatation-rotation equations using the optical flow vector. Geophysics 89 (4), S325–S337. https://doi.org/10.1190/geo2023-0198.1.
- Xu, Y.X., Xia, J.H., Miller, R.D., 2007. Numerical investigation of implementation of air-earth boundary by acoustic-elastic boundary approach. Geophysics 72 (5), SM147-SM153. https://doi.org/10.1190/1.2753831.
- Yang, T., Liu, Y.Z., Wu, Z., et al., 2023. Multi-parameter full waveform inversion using only the streamer data based on the acoustic-elastic coupled wave equation. J. Appl. Geophys. 209. https://doi.org/10.1016/j.jappgeo.2022.104902.
- Zeng, C., Xia, J.H., Miller, R.D., et al., 2012. An improved vacuum formulation for 2D finite-difference modeling of Rayleigh waves including surface topography and internal discontinuities. Geophysics 77 (1), T1–T9. https://doi.org/10.1190/geo2011-00671
- Zhang, W., Zhang, Z.G., Chen, X.F., 2012. Three-dimensional elastic wave numerical modelling in the presence of surface topography by a collocated-grid finite-difference method on curvilinear grids. Geophys. J. Int. 190 (1), 358–378. https://doi.org/10.1111/j.1365-246X.2012.05472.x.
- Zhou, X., Cao, J., Wang, G., et al., 2022. Adaptive parameter-related implementation of the free surface in elastic anisotropic full-waveform modeling. J. Appl. Geophys. 206, 104785. https://doi.org/10.1016/j. jappgeo.2022.104785.
- Zhou, X., Huo, S., Liang, Y., et al., 2023a. Finite-difference method for modeling the surface wave propagation with surface topography in anisotropic-viscoelastic media. J. Appl. Geophys. 217, 105161. https://doi.org/10.1016/j.jappgeo.2023.105161.
- Zhou, X.H., Huo, S.D., Wang, H., et al., 2023b. Model parameter design for modeling surface topography in VTI elastic finite-difference near-surface simulations. Geophysics 88 (2), C33–C52. https://doi.org/10.1190/geo2022-0027.1.
- Zhu, J.Y., Popovics, J.S., 2006. Analytical study of excitation and measurement of fluid-solid interface waves. Geophys. Res. Lett. 33 (9). https://doi.org/10.1029/ 2006g1026068.